Topological materials discovery from crystal symmetry

Benjamin J. Wieder[1,2,3]✉, *Barry Bradlyn*[4], *Jennifer Cano*[5,6], *Zhijun Wang*[7,8], *Maia G. Vergniory*[9,10,11], *Luis Elcoro*[12], *Alexey A. Soluyanov*[13,14,16], *Claudia Felser*[11], *Titus Neupert*[13], *Nicolas Regnault*[3,15] *and B. Andrei Bernevig*[3,9,10]✉

Abstract | Topological materials discovery has evolved at a rapid pace over the past 15 years following the identification of the first nonmagnetic topological insulators (TIs), topological crystalline insulators (TCIs) and 3D topological semimetals (TSMs). Most recently, through complete analyses of symmetry-allowed band structures — including the theory of topological quantum chemistry (TQC) — researchers have determined crystal-symmetry-enhanced Wilson-loop and complete symmetry-based indicators for nonmagnetic topological phases, leading to the discovery of higher-order TCIs and TSMs. The recent application of TQC and related methods to high-throughput materials discovery has revealed that over half of the known stoichiometric, solid-state, nonmagnetic materials are topological at the Fermi level, over 85 per cent of the known stoichiometric materials host energetically isolated topological bands, and just under two-thirds of the energetically isolated bands in known materials carry the stable topology of a TI or TCI. In this Review, we survey topological electronic materials discovery in nonmagnetic crystalline solids from the prediction of the first 2D and 3D TIs to the recently introduced methods that have facilitated large-scale searches for topological materials. We also discuss future venues for the identification and manipulation of solid-state topological phases, including charge-density-wave compounds, magnetic materials, and 2D few-layer devices.

Nearly 15 years have passed since the first theoretical predictions of the quantum spin Hall effect[1–3] in what are now known as 2D topological insulators (TIs). TIs, as well as topological semimetals (TSMs), are unique solid-state systems that exhibit robust boundary states and quantized bulk response coefficients as a consequence of their electronic wavefunctions. Because topological boundary states survive under moderate disorder and frequently exhibit spin polarization and spin–momentum locking, topological materials represent a promising possible platform for storing and manipulating quantum information[4–6], and realizing coherent spin transport[7–9] and high-efficiency catalysis[10–12]. Since the discovery of the first TIs, a large number of both insulating and (semi)metallic topological phases have been predicted, characterized and measured in experimentally accessible chemical compounds. This unprecedented pace of topological materials discovery has been driven by several major factors. From a theoretical perspective, the discovery of novel topological phases has been facilitated by the rapid development of topological invariants computable from band structures, and by the rediscovery and application of crystalline symmetry and group theory. The growth of topological condensed matter physics can also be attributed to the major advances in cloud storage and large-scale computing that have enabled high-throughput calculations, and to dramatic improvements in network bandwidth and digital communication that have enabled close collaboration between international teams of theorists and experimentalists.

In this work, we review topological materials discovery from the identification of the first TIs and TSMs to the modern, 'Renaissance' era of high-throughput topological classification and materials databases. For each stoichiometric 3D material discussed in this Review, we have provided the Inorganic Crystal Structure Database (ICSD)[13,14] accession code of the material with a hyperlink to the associated page on the Topological Materials Database[15,16], as well as the number and standard-setting symbol of the crystallographic space group (SG) of the material.

Owing to the sheer volume of important discoveries made since the prediction of 2D TIs, some topological materials and classifications are covered only lightly or are omitted from this Review. Interested readers may further consult a number of previous reviews[17–22]. Additionally, in this Review, we focus on the discovery

✉e-mail: bwieder@mit.edu; bernevig@princeton.edu

https://doi.org/10.1038/s41578-021-00380-2

and characterization of topology in the electronic structure of crystalline chemical compounds with weak interactions and negligible disorder. As such, we do not discuss the topological characterization of metamaterials, sonic and Floquet crystals, superconductors, classical mechanical systems, magnonic bands and strongly disordered systems, which have also seen tremendous advances in recent years.

Topological band theory

In this section, we first introduce the band theory of crystalline solids, and then detail methods through which an energetically isolated set of bands can be diagnosed as topologically nontrivial. Finally, we address experimentally observable signatures of topological bands in solid-state materials.

The band theory of crystalline solids

From a theoretical perspective, a crystal is defined as a system in which physical observables, such as the energy spectrum and the locations of atoms, are periodic under the action of discrete translations. From an experimental perspective, the picture is more complicated: samples of crystalline materials carry defects, misoriented domains, and coexisting structural orders, such as left-handed and right-handed enantiomers[23–26]. In this subsection, we focus on the underlying mathematical machinery used to characterize the electronic states in theoretical models of pristine, solid-state crystals. In the subsection 'Diagnosing band topology', we then briefly generalize to models that incorporate sources of deviation from the perfect-crystal limit, such as disorder.

To begin, in a theoretical model of a pristine, solid-state crystal, electronic phenomena are captured through a position- ($\mathbf{r}$-)space Hamiltonian that is periodic with respect to the group of 3D lattice translations[27] (FIG. 1a). In this Review, we focus on noninteracting materials, whose energy spectra and electronic response properties are largely captured in the mean-field approximation in which electron–electron correlations are either incorporated as background fields or taken to vanish. Whereas the noninteracting electronic Hamiltonian $\mathcal{H}(\mathbf{r})$ generically contains off-diagonal elements that couple states at different positions $\mathbf{r}$ and $\mathbf{r}'$, the Fourier-transformed Bloch Hamiltonian $\mathcal{H}(\mathbf{k})$ is diagonal in $\mathbf{k}$. The energy eigenvalues of the Bloch Hamiltonian $\mathcal{H}(\mathbf{k})$ form bands that are periodic with respect to advancing the crystal momentum $\mathbf{k}$ by a reciprocal lattice vector $\mathbf{G}$: $\mathbf{k} \rightarrow \mathbf{k} + \mathbf{G}$ (FIG. 1b). In $\mathbf{k}$-space, the unit cells of the reciprocal lattice are known as the Brillouin zones (BZs)[23,27]. In solid-state materials, the bands are populated by electrons up to the Fermi energy (E_F). Hence, crystals are filled with spinful fermions (electrons), even in the limit of negligible coupling between the atomic orbitals and electron spins (spin–orbit coupling, SOC).

In addition to translation symmetry, 3D crystals may respect other unitary symmetries, such as spatial inversion ($\mathcal{I}$), or antiunitary symmetries, such as time-reversal ($\mathcal{T}$). The set of symmetries that leave the orbitals (and electron spins) in an infinite crystal invariant (up to integer lattice translations) form a group; whether it is a space, layer, wallpaper, rod or another group depends on the dimensionalities of lattice translations and crystal symmetries[28]. The symmetries of nonmagnetic 3D crystals are specifically contained within the 230 nonmagnetic ($\mathcal{T}$-symmetric) SGs[27]. Crucially, unitary particle–hole (also known as chiral) symmetry, which relates the valence and conduction bands, is generically absent in real materials. The accidental or intentional incorporation of chiral symmetry into topological models is a common source of spurious predictions. Therefore, chiral symmetry, while a helpful bootstrap for forming simple models, should be carefully relaxed when predicting robust topological phenomena.

At each $\mathbf{k}$ point, bands can be uniquely labelled by the simultaneous eigenvalues (quantum numbers) of commuting unitary symmetry operations. The independent combinations of simultaneous symmetry eigenvalues can then be inferred from the symmetry operation matrix representatives in the small irreducible representations of the symmetry (little) group of each $\mathbf{k}$ point[27]. When the actions of antiunitary symmetries are incorporated, irreducible representations may become paired into irreducible corepresentations (coreps)[29,30]. In crystals with antiunitary symmetries — most notably including nonmagnetic solid-state materials — the bands at each $\mathbf{k}$ point are labelled by small coreps; the small coreps corresponding to all possible electronic states in nonmagnetic crystals were tabulated in REF.[27], and reproduced in the REPRESENTATIONS DSG tool on the Bilbao Crystallographic Server[31–34].

For a group of bands that is separated from all of the other bands in the energy spectrum by an energy gap at each $\mathbf{k}$ point, one may attempt to inverse-Fourier transform the bands into exponentially localized Wannier orbitals in position space (FIG. 1a). If a group of bands can be inverse-Fourier transformed into exponentially localized Wannier orbitals that respect the symmetries of the crystal SG, then the bands are termed Wannierizable[18,35,36]. As we discuss in the subsection 'Diagnosing band topology', the absence of

Author addresses

[1]Department of Physics, Massachusetts Institute of Technology, Cambridge, MA, USA.
[2]Department of Physics, Northeastern University, Boston, MA, USA.
[3]Department of Physics, Princeton University, Princeton, NJ, USA.
[4]Department of Physics and Institute for Condensed Matter Theory, University of Illinois at Urbana-Champaign, Urbana, IL, USA.
[5]Department of Physics and Astronomy, Stony Brook University, Stony Brook, NY, USA.
[6]Center for Computational Quantum Physics, The Flatiron Institute, New York, NY, USA.
[7]Beijing National Laboratory for Condensed Matter Physics, Institute of Physics, Chinese Academy of Sciences, Beijing, China.
[8]University of Chinese Academy of Sciences, Beijing, China.
[9]Donostia International Physics Center, Donostia/San Sebastian, Spain.
[10]IKERBASQUE, Basque Foundation for Science, Bilbao, Spain.
[11]Max Planck Institute for Chemical Physics of Solids, Dresden, Germany.
[12]Department of Condensed Matter Physics, University of the Basque Country UPV/EHU, Bilbao, Spain.
[13]Department of Physics, University of Zurich, Zurich, Switzerland.
[14]Department of Physics, St Petersburg State University, St Petersburg, Russia.
[15]Laboratoire de Physique de l'École Normale Supérieure, PSL University, CNRS, Sorbonne Université, Université Paris Diderot, Paris, France.
[16]Deceased: A. A. Soluyanov.

Wannierizability, or the properties of Wannier functions if successfully computed, are central to the identification of nontrivial band topology.

Diagnosing band topology

From a mathematical perspective, the properties of an object are considered to be topological if they do not change as the object is smoothly deformed. In some cases, symmetry-protected topological properties may also be defined by restricting consideration to objects and deformations that respect a given set of symmetries. Just under 40 years ago[37–39], it was discovered that, remarkably, the Bloch wavefunctions of energetically isolated bands in crystalline solids can carry topologically quantized numbers — known as topological invariants — that correspond to experimentally measurable quantized response effects[40]. The computation of topological invariants has allowed researchers to predict identically quantized responses in seemingly disparate solid-state materials, as well as in highly-simplified theoretical models. This is perhaps unintuitive, because the dispersion of energetically isolated bands in a material is free to change under doping, strain or in the presence of weak disorder. Hence, one might expect little correspondence between the generic properties of simple models and those of real chemical compounds. However, if the band distortion and interactions do not close a gap or break a symmetry, then the topology of the isolated bands cannot change. Because topology and symmetry alone indicate the numbers and locations of boundary states and the quantized values of bulk response coefficients in many solid-state materials, topological phenomena can be meaningfully predicted using appropriately simplified models.

Originally, nontrivial band topology was considered in the context of bulk-insulating systems[37–39]. However, the only requirement for unambiguously diagnosing the topology of a group of bands is that the bulk bands be energetically separated from the other bands in the spectrum at each momentum, such that there is a gap at each **k** point; a direct gap or an insulating, indirect gap at a particular E_F is not a prerequisite for nontrivial band topology. Hence, as first emphasized by Liang Fu and Charles Kane in establishing the nontrivial band topology of metallic antimony [ICSD 426972, SG 166 ($R\bar{3}m$)][41], it is also possible to classify metallic materials as topological band insulators. In this Review, we specifically define a band insulator as a material with N_e electrons per unit cell in which the N_e lowest-energy Bloch eigenstates at each **k** point are separated from all higher-energy Bloch eigenstates at **k** by a gap. Therefore, we employ the convention established in REF.[41], in which a material is classified as a TI or a TCI if the lowest N_e bands in energy are, as a set, topological, even if there are bulk electron or hole Fermi pockets.

Topological material predictions are reliable because topological robustness is an extensive property: the larger the size of the topological bulk of a system in real space, the more robust the bulk topology is to interactions and disorder that preserve the system symmetry, on average. This property crucially allows topological response effects and boundary states in simplified models of pristine crystals to be generalized to real-material samples, which inevitably host inhomogeneities such as crystal defects, dopants and reconstructed surface textures[23–25]. For Chern insulators, extensive topological robustness has been demonstrated using network models[42–44] and renormalization group flow[45]. More recently, similar calculations were also performed to extract the critical conductance and correlation lengths of the Anderson localization transition in TIs and TCIs[46–51].

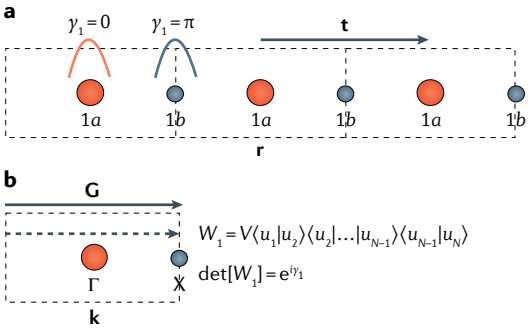

Fig. 1 | **Wannier centres and Wilson loops. a** | A 1D crystal in position (**r**) space, where adjacent unit cells (black dashed rectangles) are related through lattice translation by the vector **t**. The orange and grey curves at the 1*a* and 1*b* Wyckoff positions in the leftmost unit cell symbolize exponentially localized, inversion ($\mathcal{I}$)-symmetric Wannier orbitals[18,35,36] obtained from inverse-Fourier-transforming bands with a Berry phase[63] (equivalently termed a Zak phase[64]) $\gamma_1 = 0$ and $\gamma_1 = \pi$, respectively. **b** | **k** points in the first Brillouin zone (BZ) of the 1D crystal in **a** are related to **k** points in the second BZ by the reciprocal lattice vector **G**. For a set of occupied bands $|u_{\mathbf{k}}\rangle$ at each point **k** in the first BZ, the discretized Wilson loop matrix W_1 is defined as the product of the outer products of $|u_{\mathbf{k}}\rangle$ and $|u_{\mathbf{k}+1}\rangle$ taken in the direction of the dashed arrow over a finite mesh of **k** points in the first BZ (as well as a sewing matrix V)[71–74]. Crucially, for an energetically isolated set of bands, the total Berry phase $\gamma_1 \bmod 2\pi$ is related to the Wilson loop matrix by $\det[W_1] = \exp(i\gamma_1)$.

Classes of topological bands. Heuristically, there are three broad classes of topological bands in solid-state materials: obstructed atomic limits, fragile bands and stable topological bands. First, in obstructed atomic limits, the isolated bands are Wannierizable, but the Wannier centres reside at positions in the unit cell away from the underlying atomic ions[31,52]. Consequently, obstructed atomic limits exhibit electric multipole moments[36,53], and boundaries between atomic limits and obstructed atomic limits exhibit either 0D or flat-band-like topological solitons with fractional charge or spin–charge separation[54]. In 1D, Wannier functions are always exponentially localized[55] in the absence of superconductivity[56], and hence, all topological phases are obstructed atomic limits. However, in 2D and 3D, one must be more careful in constructing Wannier functions, as topological bands in 2D and 3D may admit a localized **r**-space description with power-law decaying tails, as opposed to the exponential decay required for Wannierizability[57–59]. Topologically quantized charge and spin on domain walls between atomic limits were

first identified in the Su–Schrieffer–Heeger[60,61] and Rice–Mele[62] models of polyacetylene. In the Su–Schrieffer–Heeger model, there are two insulating regimes whose occupied bands differ by a π Berry[63] phase — equivalently termed a Zak[64] phase — that indicates the relative positions of the occupied Wannier orbitals[36,53] (FIG. 1a).

More recently, the polarization topology of obstructed atomic limits was extended to quadrupole and octupole moments through a formulation of nested Berry phase[59,65–70]. First, for a set of occupied bands $|u_{\mathbf{k}}\rangle$ at each point $\mathbf{k}$ in the first BZ, one may define a discretized Wilson loop matrix W_1 as the product of the outer products of $|u_{\mathbf{k}}\rangle$ and $|u_{\mathbf{k+1}}\rangle$ taken over a finite mesh of $\mathbf{k}$ points in the first BZ (as well as a sewing matrix V)[71–74]. The total Berry phase γ_1 mod 2π of the occupied bands is then related to the Wilson loop matrix by $\det[W_1] = \exp(i\gamma_1)$ (FIG. 1b). In this sense, the Wilson loop W_1 represents the non-Abelian (many-band) generalization of the Berry phase[57,58,71–78]. It was recently recognized that because the eigenvalues of W_1 form smooth and continuous bands, then a second, nested Wilson loop matrix W_2 may be constructed by computing a perpendicular Wilson loop using the eigenstates of W_1. Analogous to the relationship between the Berry phase γ_1 and W_1, a nested Berry phase γ_2 can then be defined through the relation $\det[W_2] = \exp(i\gamma_2)$[59,65–70]. The nested Berry phase γ_2 was first introduced to diagnose the topology of quantized quadrupole insulators, in which $\gamma_2 = 0, \pi$ indicates whether a pair of Wannier orbitals occupy the corner or the centre of a 2D square lattice[65,66,68,79]. Additionally, 3D obstructed atomic limits have recently been predicted in silicon crystals [ICSD 150530, SG 227 ($Fd\bar{3}m$)][80] and in electrides including Y_2C [ICSD 672345, SG 166 ($R\bar{3}m$)][81], $Li_{12}Al_3Si_4$ [ICSD 39597, SG 220 ($I\bar{4}3d$)][82], and Ca_2As [ICSD 166865, SG 139 ($I4/mmm$)][83,84]. The theory of topological quantum chemistry (TQC)[31,32,58,85–87], which we discuss in detail in the section 'Topological quantum chemistry and symmetry-based indicators', is built upon the complete enumeration of atomic limits in the 230 nonmagnetic SGs. In this Review, we primarily discuss the boundary states of obstructed atomic limits in the context of the flat-band-like surface and hinge states of TSMs.

It was recently discovered[58,85,88–91] that, in some cases, a group of bands exhibits boundary solitons[59,68,69,92–95], but does not admit a Wannier description unless combined with other, trivial (Wannierizable) bands. These fragile topological bands have been shown to lie close to E_F in hundreds of solid-state materials[16], and to be relevant to the low-energy excitations in twisted bilayer graphene[96–98].

The last class of bands–and the most ubiquitous[16]–exhibit the stable topology of TIs and TCIs. Stable topological bands, unlike fragile bands or obstructed atomic limits, cannot be Wannierized, and remain non-Wannierizable when combined with (obstructed) atomic limits or fragile bands. However, stable topological bands can generically be partially Fourier-transformed into hybrid Wannier functions with one coordinate $r_\perp$ in position space perpendicular to two components $\mathbf{k}_\parallel$ in momentum space[18,35,99–101]. As first discovered by David Thouless, Mahito Kohomoto, Peter Nightingale, and Marcel de Nijs[37–39] in the 1980s, in stable TIs and TCIs, the positions of the hybrid Wannier functions necessarily wind as functions of $\mathbf{k}_\parallel$. In a 2D quantum Hall phase considered in the limit of a rational flux quantum per unit cell such that there exists a 2D Bravais lattice of commuting (magnetic) translations[102], Thouless, Kohomoto, Nightingale, de Nijs, and other researchers[103] recognized that the hybrid-Wannier-centre winding can be classified by an integer-valued topological invariant termed a Chern number. Crucially, the Chern number of a set of bands cannot be changed without closing a gap between the bands and other bands in the spectrum. Additionally, the Chern number of all of the occupied bands corresponds to the bulk Hall conductivity σ_H^{xy} in the units of e^2/h, as well as to the number of topological chiral edge states.

After the discovery of the integer quantum Hall effect in 2D Chern insulators[40], a wide variety of topological response effects have been theoretically proposed and experimentally verified in systems with higher symmetry or dimensionality, including TIs and TCIs (FIG. 2). Unlike in Chern insulators, the hybrid-Wannier winding in TIs and TCIs — known as spectral flow because of its correspondence to the infinite 'flowing' connectivity of topological boundary states[71] — is enforced by additional symmetries. Specifically, when combinations of spatial and $\mathcal{T}$ symmetries are relaxed in TIs and TCIs, the spectral flow may be removed (trivialized), and the bulk topology reduced to that of a fragile TI or an (obstructed) atomic limit.

Wilson loops. Numerous, equivalent methods have been introduced to diagnose the topology of TIs and TCIs[1–3,57,75,104–109]. However, most methods cannot be generalized to realistic models of real-material band structures with varying symmetries, complicated dispersion, and large numbers of occupied bands. To date, the most consistently reliable and generalizable means of diagnosing single-particle band topology is the Wilson loop method discussed earlier in this section[57,58,71–78] (FIG. 1b). When calculated over an energetically isolated set of bands in two or more dimensions, the Wilson loop eigenvalues indicate the $\mathbf{k}_\parallel$-dependent locations $r_\perp$ of the hybrid Wannier orbitals. Hence, the appearance of a winding Wilson spectrum either indicates stable spectral flow or fragile topology. A nested Wilson loop method[59,65–69] was also recently introduced to calculate higher-order (hinge) spectral flow in three or more dimensions, which we further detail in the section 'Higher-order TCIs and TSMs'.

Because the (nested) Wilson loop eigenvalues, when calculated over bands that are not fragile topological, correspond to the surface (hinge) spectrum of a crystal[57–59,65–69,71–78], Wilson-loop calculations have emerged as a highly accurate means of identifying and classifying the stable topology of real materials. Implementing the formulations in REFS[71–73], researchers have released publicly available packages for calculating the Wilson loops of tight-binding models[110] and ab initio electronic structures[100]. However, the Wilson-loop method has major drawbacks that largely prevent its

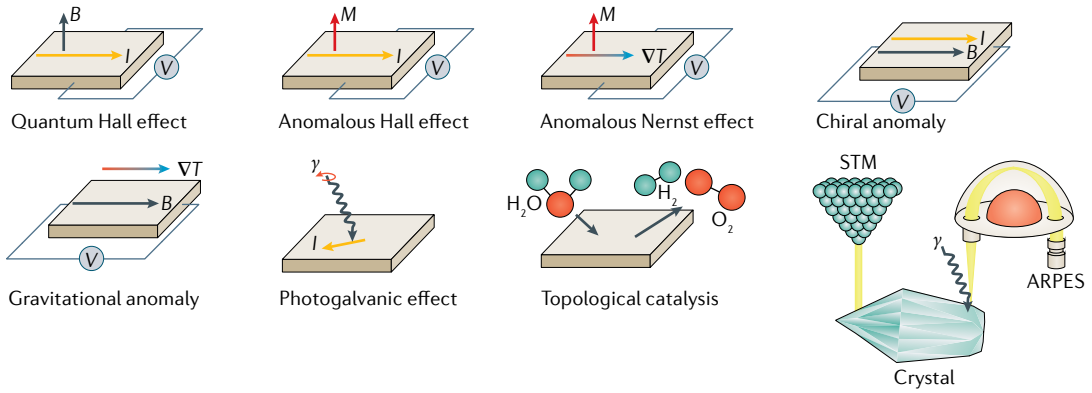

Fig. 2 | **Experimentally verified topological response effects in topological materials.** In the response effect schematics, B is an external magnetic field, M is the magnetization, I is the electric current, V is the voltage, T is the temperature, and γ is a photon. Notable topological response effects include the quantum Hall effect (quantized V induced by perpendicular I and B)[40], the anomalous Hall effect (V induced by perpendicular I and M)[125,396,397], the anomalous Nernst effect (V induced by perpendicular ∇T and M)[24,398–401], the chiral anomaly (I induced by parallel V and B)[243–250,402], the gravitational anomaly (V induced by parallel ∇T and B)[241,242], the photogalvanic effect (I induced by incident light)[290,291,293,294,368,403,404] and topologically enhanced catalysis (chemical reaction efficiency enhancement from topological surface states)[10–12]. In 3D solid-state materials, experimental signatures of topological response effects are frequently bolstered by the concurrent observation of topological surface states in angle-resolved photoemission spectroscopy (ARPES)[153,154] and scanning-tunnelling microscopy (STM)[155,228,367,405,406] experiments.

automation in large-scale materials discovery. First, to compute the Wilson loop for a 3D material, one must calculate the occupied eigenstates on a 2D manifold of the BZ using a very dense mesh of **k** points, which is demanding in terms of both memory and processing time. Second, because Wilson loops are path-dependent, their implementation requires the manual input of a **k**-path specifically chosen to diagnose a particular topological phase. For example, to identify the glide-protected hourglass TCI phase in KHgSb [ICSD 56201, SG 194 ($P6_3/mmc$)][76,77] and the fourfold Dirac TCI phase in Sr_2Pb_3 [ICSD 648570, SG 127 ($P4/mbm$)][78], researchers implemented a complicated, glide-resolved Wilson loop that bent along perpendicular planes in the BZ. A bent Wilson loop was also recently employed to identify Weyl TSM phases in materials with fourfold rotoinversion symmetry[111,112].

Symmetry-based indicators. Unlike (nested) Wilson loop calculations, symmetry-based indicators of band topology (SIs)[113–115], such as the Fu–Kane parity criterion[41], require only the determination of the eigenvalues of the occupied bands at high-symmetry BZ points, and are therefore computationally efficient and generalizable to large families of materials with the same symmetries. As more elaborate TI and TCI phases have been discovered, the set of Fu–Kane-like SIs of stable topology has continued to grow. In the section 'Topological quantum chemistry and symmetry-based indicators', we discuss how the discoveries of TQC and related methods were exploited to compute the complete SIs of the 230 nonmagnetic SGs[67,116–121], and facilitated recent large-scale efforts to identify nonmagnetic topological materials[15,16,122–124].

It is important to emphasize that SIs generically provide an incomplete characterization of bulk topology. For example, the n-fold-rotation SIs introduced in REF.[114] only specify the $\mathbb{Z}$-valued Chern number up to the integer n. Additionally, there are large numbers of materials, such as noncentrosymmetric crystals, whose SGs do not carry eigenvalue indicators[117,119]. Therefore, for many crystal structures and materials, the (nested) Wilson loop remains the only complete means of identifying the bulk topology. Recently, for example, the higher-order TCI phases of noncentrosymmetric γ-$MoTe_2$ and γ-WTe_2 crystals [ICSD 14348, SG 31 ($Pmn2_1$)] were identified through the computation of a nested Wilson loop[69].

The first topological insulators

Over 20 years passed between the characterization of Chern insulators and polyacetylene and the discovery of the first $\mathcal{T}$-symmetric TIs. In a key intermediate step, Duncan Haldane in 1988 formulated a model of a Chern insulator in a crystal with a periodic — but net-zero — magnetic field[125]. Like all Chern insulators, the Haldane model exhibits 1D chiral edge modes. In 2004, when constructing tight-binding models of graphene[126], Kane and Eugene Mele formulated a model of a 2D TI that, when the nearly vanishing effects of SOC are incorporated, reduces to two, time-reversed copies of the Haldane model. Hence, the Kane–Mele model exhibits helical edge modes[1]. Crucially, Kane and Mele deduced that the helical edge modes are prevented from gapping by $\mathcal{T}$ symmetry[1,2]. A more realistic formulation of 2D TIs in HgTe quantum wells was introduced shortly afterwards by Andrei Bernevig, Taylor Hughes and Shou-Cheng Zhang[3], and was subsequently confirmed through transport measurements[127]. Bernevig, Hughes and Zhang also crucially identified band inversion as a general mechanism for obtaining topological phases[3].

In both the Kane–Mele and Bernevig–Hughes–Zhang models of 2D TI phases, the bulk topology can

be deduced by a $\mathbb{Z}_2$ invariant that tracks the helical winding of the partial polarization, or the Berry phase per half of the occupied states[2,75]. However, in practice, the Kane–Mele $\mathbb{Z}_2$ invariant is exceedingly difficult to compute in realistic models, as it requires a careful treatment of matrix square roots and Pfaffians, as well as the computationally intensive process of determining, storing and integrating the occupied states at each **k** point. Although a handful of calculations based on the Kane–Mele Pfaffian invariant have been employed to diagnose the topology of TI and TCI models[128,129], the numerical prediction of TI and TCI phases in real materials without SIs has primarily been accomplished through the equivalent Wilson-loop method introduced in REFS[71–73]. Since the prediction by Bernevig, Hughes, and Zhang of 2D TI phases in HgTe quantum wells, 2D TI phases have been predicted in monolayers of jacutingaite (Pt_2HgSe_3)[130], predicted and experimentally explored in monolayers of bismuth[128,131–133] and monolayers of the transition-metal dichalcogenide (TMD) MoS_2[134], and have been predicted and experimentally confirmed in monolayers of WTe_2 (REFS[135–137]) and $Ta_2Pd_3Te_5$ (REFS[138,139]). Notably, Pt_2HgSe_3 realizes a weak TI phase when stacked into 3D structures[140–142], as we discuss below, whereas bismuth[116] and the TMDs $MoTe_2$ and WTe_2 (REFS[69,123,124]) become higher-order TCIs with 1D helical hinge modes when stacked into 3D.

The foundation for topological material discovery in 3D solid-state materials was most firmly established in 2006, when several independent groups predicted the existence of 3D TIs. In 3D TIs, the bulk topology is characterized by a 3D $\mathbb{Z}_2$ invariant, and each surface exhibits an unpaired (anomalous) twofold Dirac cone[41,104,105,143,144]. In particular, Fu and Kane crucially recognized that if a 3D TI is also symmetric under the exchange of spatial coordinates — known as spatial inversion ($\mathcal{I}$) or parity symmetry — then the $\mathbb{Z}_2$ invariant can simply be deduced from the bulk parity eigenvalues of the occupied bands at the $\mathcal{T}$-invariant **k** (TRIM) points[41]. Because the integral formulation of the 3D $\mathbb{Z}_2$ invariant is even more mathematically and computationally intensive than its 2D counterpart[41,104,143], it provided little help towards predicting 3D TI phases in real materials. Conversely, the Fu–Kane parity criterion immediately provided a simple recipe for discovering centrosymmetric 3D TIs: generalizing the earlier link between TI phases and band inversion recognized by Bernevig, Hughes and Zhang, Fu and Kane predicted 3D TI phases in insulating compounds with odd numbers of band inversions at TRIM points between bands with opposite parity eigenvalues. Fu, Kane, and Mele then specifically proposed a band-inversion-driven 3D TI in $Bi_{1-x}Sb_x$ alloys, whose characteristic anomalous surface states were shortly afterwards measured in experiment[145,146] (FIG. 3a). In the following years, more idealized 3D TI phases were identified in Bi_2Se_3 [ICSD 42545, SG 166 ($R\bar{3}m$)], Bi_2Te_3 [ICSD 617192, SG 166 ($R\bar{3}m$)], Sb_2Te_3 [ICSD 193346, SG 166 ($R\bar{3}m$)], and $Bi_{2-\delta}Ca_\delta Se_3$ crystals[147–152] (FIG. 3b). These 3D TI phases were initially observed in angle-resolved photoemission spectroscopy (ARPES) experiments[153,154], and anomalous Dirac-cone surface states in 3D TIs were subsequently confirmed through quasiparticle interference in scanning tunnelling microscopy (STM) experiments[155].

Last, concurrently with the prediction of 3D TIs, researchers also proposed the existence of weak 3D TIs. From a theoretical perspective, weak TIs can be deformed into position-space stacks of 2D TIs that contain one 2D TI layer in each stack unit cell, where the normal vector of each 2D TI layer is oriented along the $(Z_{2,1}\hat{\mathbf{x}} + Z_{2,2}\hat{\mathbf{y}} + Z_{2,3}\hat{\mathbf{z}})$-direction (the stacking direction)[41,105,143,144]. The three $\mathbb{Z}_2$-valued indices $Z_{2,i}$ are termed the weak indices, and the stacking direction $(Z_{2,1}, Z_{2,2}, Z_{2,3})$ is termed the weak-index vector. Weak TIs owe their name to the recognition that in samples with even numbers of layers, all of the 2D TI helical modes may pairwise annihilate, rendering the weak TI sample devoid of topological boundary states[156]. Hence, few-layer weak TI samples are expected to exhibit a layer-dependent 2D quantum spin Hall effect[41,105,143,144,156,157]. Weak TI phases have been predicted and experimentally confirmed through ARPES probes in BiI [ICSD 1559, SG 12 ($C2/m$)][158,159], Pt_2HgSe_3 [ICSD 185808, SG 164 ($P\bar{3}m1$)][140–142], and strained $ZrTe_5$ [ICSD 85507, SG 63 ($Cmcm$)][160,161]. A weak TI phase was also engineered in a graphene-like layered structure of $Bi_{14}Rh_3I_9$[162], as confirmed through bulk ARPES probes[163] and STM experiments demonstrating the presence of step-edge helical modes[164]. Most recently, a weak TI phase was identified through first-principles and ARPES investigations[165] of a relatively unstudied structure of $RhBi_2$ that is not recorded in the ICSD[13,14,166].

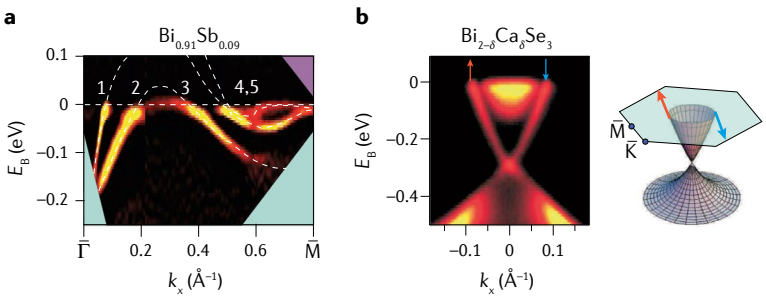

Fig. 3 | **The twofold Dirac-cone surface states of 3D topological insulators.** **a** | The dispersion of the surface states in $Bi_{1-x}Sb_x$ measured through angle-resolved photoemission spectroscopy (ARPES) experiments as the electron binding energy (E_B) at varying k_x (REF.[146]). The surface bands cross the Fermi level (horizontal dashed white line) an odd number of times, indicating the spectral flow of a 3D topological insulator, as predicted in REFS[41,104,143]. **b** | The unpaired Dirac-cone surface state of Ca-doped Bi_2Se_3 [ICSD 42545, SG 166 ($R\bar{3}m$)] measured by spin-resolved ARPES (left), with a schematic depicting the time-reversal-symmetric spin texture of the topological Dirac-cone surface states (right). Red and blue arrows indicate spin up and down, respectively. Panel **a** reprinted with permission from REF.[146], AAAS. Panel **b** reprinted from REF.[150], Springer Nature Limited.

Topological crystalline insulators

When searching for candidate 3D TIs, Fu and Kane initially suggested that $Pb_{1-x}Sn_x$ Te alloys exhibited a 3D TI phase separated by two equally trivial insulators: PbTe [ICSD 648585, SG 225 ($Fm\bar{3}m$)] and SnTe [ICSD 601065, SG 225 ($Fm\bar{3}m$)][41]. However, it was quickly realized[167], and subsequently confirmed through ARPES experiments[168] (FIG. 4a,b), that SnTe is in fact not a trivial insulator. Rather, SnTe was recognized to be

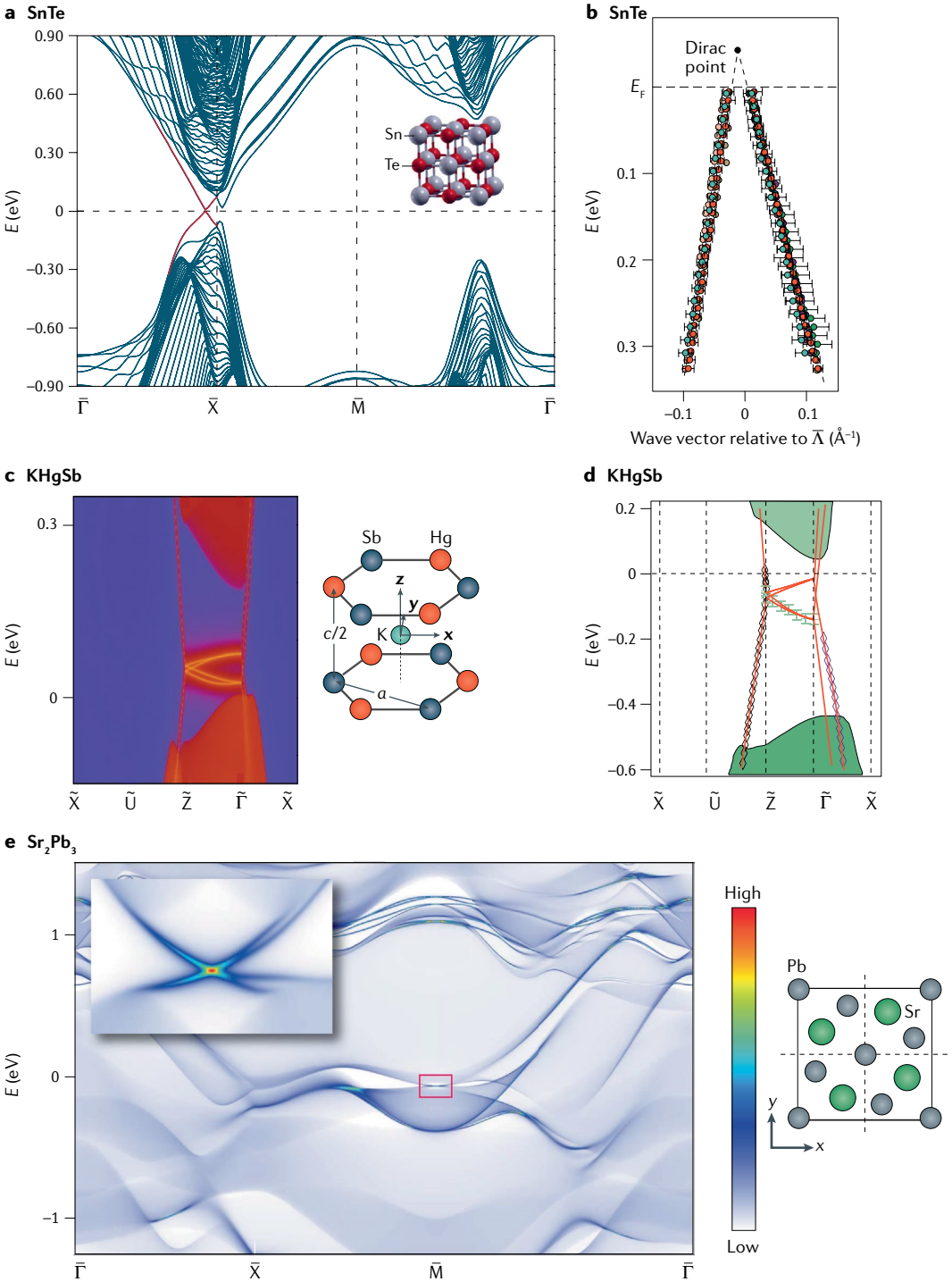

Fig. 4 | **3D topological crystalline insulators. a** | A tight-binding calculation predicting the presence of twofold Dirac-cone surface states (crossing red bands) in the mirror topological crystalline insulator (TCI) SnTe [ICSD 601065, SG 225 ($Fm\bar{3}m$)][167,168]. **b** | Angle-resolved photoemission spectroscopy (ARPES) data for various photon energies confirming the existence of surface Dirac cones in the TCI SnTe, plotted along a line of surface mirror symmetry ($\bar{\Gamma}\bar{X}$) and centred at the surface Dirac cone at $k_x = \bar{\Lambda}$. The error bars in **b** reflect the uncertainties originating from the momentum resolution and the standard deviation in the peak positions in the ARPES data. **c** | Topological hourglass surface fermions in the glide TCI KHgSb [ICSD 56201, SG 194 ($P6_3/mmc$)][76,77,176,177], calculated from first principles. **d** | ARPES data supporting the existence of topological hourglass surface states in KHgSb. **e** | Anomalous fourfold Dirac-cone surface states in the nonsymmorphic Dirac TCI Sr_2Pb_3 [ICSD 648570, SG 127 ($P4/mbm$)], calculated from first principles. The colour bar indicates the computed surface spectral weight in arbitrary units, which is high for the fourfold Dirac cone in the red rectangle at $\bar{M}$ near $E = 0$ (shown in closer detail in the inset panel). Panel **a** reprinted from REF.[167], Springer Nature Limited. Panel **b** reprinted from REF.[168], Springer Nature Limited. Panel **c** reprinted from REF.[77], Springer Nature Limited. Panel **d** adapted with permission from REF.[176], AAAS. Panel **e** reprinted with permission from REF.[78], AAAS.

a new variant of 3D TI — a 3D TCI — in which the Fu–Kane–Mele 3D $\mathbb{Z}_2$ invariant is trivial, and the bulk stable topology is instead protected by mirror symmetry (as well as bulk fourfold rotation symmetry[67,118,169]). In SnTe, there are even numbers of twofold Dirac-cone surface states lying along surface lines of mirror symmetry[167]. More broadly, in TCIs, the bulk topology is enforced by specific combinations of unitary symmetries, such as mirror reflection, and antiunitary symmetries, such as $\mathcal{T}$. Anomalous topological surface states consequently manifest on crystal facets whose 2D symmetry (wallpaper) groups include the projections of the 3D symmetries that protect the bulk topology[78,170–173].

After the discovery of mirror TCIs, researchers proposed nonsymmorphic TCI phases protected by bulk glide reflection[76–78,174,175]. In magnetic Möbius TCIs[174,175], unpaired Dirac-cone surface states — like those of 3D TIs — appear along surface glide lines. In $\mathcal{T}$-symmetric hourglass TCIs[76–78] — which are topologically equivalent to time-reversed, superposed pairs of Möbius TCIs — the surface bands cross in hourglass-like connectivities along surface glide lines, forming pairs of twofold Dirac cones (FIG. 4c,d). Most recently, an exotic, nonsymmorphic Dirac insulator phase with an anomalous fourfold surface Dirac cone — twice the degeneracy of a 3D TI surface state — was proposed in crystals with two perpendicular, surface-projecting glide planes (FIG. 4e)[78]. An hourglass TCI phase was predicted[76,77] and incipiently confirmed through ARPES[176] and quantum oscillations[177] in KHgSb [ICSD 56201, SG 194 ($P6_3/mmc$)] (FIG. 4c,d). Shortly afterwards, an hourglass TCI phase was also predicted in $Ba_5In_2Sb_6$ [ICSD 62305, SG 55 ($Pbam$)], and a nonsymmorphic Dirac TCI phase was predicted in Sr_2Pb_3 [ICSD 648570, SG 127 ($P4/mbm$)] (FIG. 4e)[78]. From a bulk perspective, it is important to note that whereas centrosymmetric mirror TCIs may be identified through SIs[114,117,119,120], nonsymmorphic TCIs may only be identified by performing a Wilson loop or equivalent calculation[76–78,119,174,175].

Recently, researchers have also discovered the existence of 3D higher-order TCIs (HOTIs), which are characterized by gapless 1D hinge states that sometimes coexist with 2D surface Dirac cones. Specifically, although the lowest-symmetry HOTI models exhibit gapped 2D surfaces and gapless 1D hinges[69,117,119,120], typical solid-state HOTIs have additional crystal symmetries that can protect gapless 2D surface states. Hence, classifying a typical solid-state TCI as a HOTI or as a first-order TCI is in practice a matter of preference: depending on the sample termination, the same crystal may exhibit topological surface states or gapped facets separated by topological hinge states. For example, the first observed mirror TCI–SnTe–has recently been reclassified as a HOTI[15,67,119,122–124]. Specifically, when bulk or surface mirror symmetry is relaxed in SnTe by strain or sample termination while preserving fourfold rotation symmetry, the surface states are no longer protected by mirror symmetry (though some surface states remain protected by the product of twofold rotation and $\mathcal{T}$ symmetry[169]). In SnTe samples with broken mirror symmetry, the hinges between facets with gapped surface states are predicted to bind 1D helical modes[67,118,119,169]. Furthermore, first-principles calculations have suggested that PbTe [ICSD 648588, SG 225 ($Fm\bar{3}m$)] — which is isostructural to SnTe — may also realize TCI and HOTI phases depending on sample quality and preparation details[15,122–124,178]. Last, other TCI phases — most notably including nonsymmorphic Dirac TCIs — also represent the parent phases of HOTIs with helical hinge states[69,78,179,180].

Topological semimetals

Historically, the term semimetal has been used to describe solid-state materials in which there is a small but non-zero density of states at E_F (REF.[23]). However, there are two distinct mechanisms for realizing a semimetallic density of states. In the first case, such as in the archetypal semimetal bismuth [ICSD 64703, SG 166 ($R\bar{3}m$)][181], there is a gap at all **k** points, but the system remains metallic owing to its negative indirect bandgap. As emphasized by Fu and Kane[41], bismuth-like semimetals may still exhibit nontrivial band topology owing to the presence of an energy gap between the valence and conduction manifolds at all **k** points. Hence, in more modern literature, semimetals like bismuth are referenced as band insulators. In recent years, bismuth itself was in fact recognized to be a higher-order topological crystalline band insulator[116].

In the second case, a semimetallic density of states occurs in crystalline solids in which the bulk bands meet at E_F in only a handful of nodal points, but are otherwise separated by an energy gap. Such systems are termed nodal semimetals. The prototypical 2D nodal semimetal phase occurs in graphene, in which the spin-degenerate bands meet in only two, linearly dispersing points[126,182–184]. If the bands in a d-dimensional (d-D) nodal semimetal exhibit nontrivial (d−1)-D or (d−2)-D polarization, fragile or stable topology, then the nodal semimetal is further classified as a topological semimetal (TSM). For example, in zigzag-terminated graphene, the edge **k** points between the projections of the bulk nodal points exhibit nearly flat bands enforced by bulk polarization topology[185–188]; hence, graphene is the simplest TSM. Because the low-energy mathematical description of the nodal points in graphene (the **k**·**p** Hamiltonian) resembles the Dirac equation for relativistic particles[183,184], the nodal points were termed 2D Dirac points. As we discuss in the subsection 'Dirac and Weyl semimetals', in 3D TSMs, there can exist bulk nodal degeneracies whose **k**·**p** Hamiltonians resemble the high-energy Dirac and Weyl equations; hence, in these 3D TSMs, the nodal points are termed 3D Dirac and Weyl points, respectively. Initially, the search for TSMs and TIs was motivated as an effort to observe condensed-matter realizations of high-energy phenomena. For example, the surface states of 3D TIs are unpaired twofold Dirac cones, representing half of the degeneracy of each of the Dirac points in graphene[41,104,143,145,189]. From the perspective of high-energy theory, the unpaired Dirac cones on 3D TI surfaces represent experimentally observable topological exceptions to the parity anomaly: a fermion-doubling theorem that was first formulated in the context of high-energy models that requires symmetry-stabilized twofold Dirac cones to appear in

pairs in 2D systems[190–192]. However, as we discuss in the subsection 'Unconventional TSMs and chiral crystals', researchers have since discovered numerous 3D solid-state TSMs in which the nodal degeneracies at E_F are neither Dirac nor Weyl fermions.

Dirac and Weyl semimetals

For a time, the analogy between solid-state and high-energy physics held relatively well in 3D semimetals. Searching for 3D generalizations of graphene, researchers identified 3D Dirac semimetals through two, parallel tracks. First, researchers recognized that nodal fermions at high-symmetry **k** points transform in small coreps of the little group $G_{\mathbf{k}}$[193,194]. Because the small coreps of the little groups in all 230 nonmagnetic SGs were enumerated in REF.[27], it was possible to target specific **k** points in specific SGs for high-symmetry-point, essential 3D Dirac fermions: fourfold degeneracies with linear dispersion in all three directions that transform in four-dimensional, double-valued small coreps at high-symmetry BZ points. More broadly, essential nodal points were recognized to be features of the minimal band connectivity in each SG, and can also lie along high-symmetry lines and planes in nonsymmorphic and non-primitive SGs[195–197]. Searching for high-symmetry-point, essential Dirac fermions, researchers theoretically predicted 3D Dirac semimetal phases in hypothetical, metastable structural phases of the BiO_2[194] and $BiZnSiO_4$ families[198]. Unfortunately, the structural phases of BiO_2 and $BiZnSiO_4$ in REFS[194,198] have thus far proved to be experimentally inaccessible. Nevertheless, high-symmetry-point, essential nodal fermions have since been discovered in a wealth of readily accessible materials, validating the methods introduced in REFS[193,194]. Furthermore, REFS[194,198] represented some of the earliest attempts at combining crystal symmetry, group theory and materials databases for topological materials discovery, laying the foundation for large-scale materials discovery efforts.

Other researchers hunted for solid-state realizations of 3D Dirac fermions along a second, parallel research track focused on band inversion. Unlike high-symmetry-point Dirac fermions, band-inversion 3D Dirac fermions are defined as fourfold degeneracies with linear dispersion in all three directions that form at the crossing points between two, twofold-degenerate bands that transform in different small coreps of a little group along a high-symmetry BZ line or plane. In band-inversion semimetals, unlike in essential, high-symmetry-line or plane semimetals, the nodal points at E_F are not required to be present in the minimal band connectivity, and are instead pairwise nucleated by band inversion. Searching for compounds in which the bulk bands were strongly inverted along axes of fourfold or sixfold rotation symmetry, researchers predicted band-inversion 3D Dirac semimetal phases in Cd_3As_2 [ICSD 609930, SG 137 ($P4_2/nmc$)][199] and Na_3Bi [ICSD 26881, SG 194 ($P6_3/mmc$)][200], which were concurrently confirmed in ARPES experiments[201–204]. Tilted (type-II) variants of band-inversion Dirac TSM phases have also been proposed in the VAl_3 [ICSD 167811, SG 139 ($I4/mmm$)][205] and YPd_2Sn [ICSD 105699, SG 225 ($Fm\bar{3}m$)][206] material families, and observed in $PtTe_2$ [ICSD 649753, SG 164 ($P\bar{3}m1$)] through ARPES experiments[207].

During their initial characterization, the designation of Dirac semimetals as TSMs was controversial. Specifically, on the one hand, it was recognized that Dirac semimetals could exhibit arc-like surface states[208–211], and that the same band inversions that create Dirac points can also result in high-symmetry BZ planes exhibiting the same stable bulk topology and surface states as 2D TIs and TCIs[212]. Indeed, arc-like surface states were experimentally observed in Dirac semimetal phases in Cd_3As_2, Na_3Bi and $PtSn_4$ [ICSD 54609, SG 68 ($Ccce$)] through ARPES[208,209,213], quantum oscillations[210,214] and quasiparticle interference in STM[215,216]. However, on the other hand, it was also recognized that the arc-like states were not topological[217], and that not all Dirac semimetals are required to exhibit surface states[218,219]. Recently, it was discovered that large families of Dirac semimetals, including Cd_3As_2, exhibit higher-order hinge states as a direct topological consequence of their bulk Dirac points, definitely resolving the status of Dirac semimetals as TSMs[68].

In addition to 3D Dirac fermions, researchers also discovered solid-state realizations of conventional Weyl fermions, defined as twofold degeneracies with linear dispersion in all three directions[220–222]. Unlike Dirac fermions, conventional Weyl fermions carry a nontrivial topological invariant in the absence of symmetry — the Chern number $|C| = 1$ evaluated on a sphere around the Weyl point (also known as the chiral charge of the Weyl point) — and hence can form at any point in the BZ of a crystal with singly-degenerate bands, even if the crossing bands are labelled with the same small coreps. More generally, Weyl points are condensed-matter realizations of chiral fermions: nodal degeneracies with nontrivial, $\mathbb{Z}$-valued monopole (chiral) charges reflecting the difference in the Chern number evaluated in 2D BZ planes above and below the chiral fermion. On the 2D facets of finite crystals with Weyl points at E_F, the projections of BZ planes with nontrivial Chern numbers host topological surface Fermi arcs that span the projections of the bulk chiral fermions[221]. A conventional Weyl semimetal is therefore the simplest variant of a chiral TSM: a gapless phase of matter in which some or all of the bulk Fermi pockets carry nontrivial chiral charges. Chiral TSMs can hence be contrasted with achiral TSMs — such as Dirac semimetals — in which none of the bulk Fermi pockets originate from chiral fermions with uncompensated chiral charges.

The first Weyl semimetals were predicted in magnetic phases of pyrochlore iridates like $Y_2Ir_2O_7$ [ICSD 187534, SG 227 ($Fd\bar{3}m$)][221], although Weyl points have not yet been observed in these materials. Shortly after the discovery of 3D Dirac semimetals, band-inversion Weyl-semimetal phases were predicted[223,224] and experimentally confirmed through ARPES[225–227] and quasiparticle interference in STM[228] in the transition-metal monophosphides TaAs [ICSD 611451, SG 109 ($I4_1md$)], TaP [ICSD 648185, SG 109 ($I4_1md$)], NbAs [ICSD 16585, SG 109 ($I4_1md$)], and NbP [ICSD 81493, SG 109 ($I4_1md$)]. Type-II (tilted) Weyl

points were also predicted to lie near E_F in the noncentrosymmetric, isostructural TMDs γ-WTe_2 [ICSD 14348, SG 31 ($Pmn2_1$)][229] and γ-$MoTe_2$ (REF.[230]), although later research[69] has suggested that 3D TMDs may also be HOTIs. Higher-charge Weyl points stabilized by rotation symmetries have additionally been proposed in $SrSi_2$ [ICSD 24145, SG 212 ($P4_332$)][231], $NbSi_2$ [ICSD 601659, SG 180 ($P6_222$)][232], and in the ferromagnetic phase of $HgCr_2Se_4$ [ICSD 626175, SG 227 ($Fd\bar{3}m$)][233,234].

Though most Weyl points near E_F in solid-state materials arise from band inversion, researchers have also recently predicted essential Kramers–Weyl points pinned to TRIM and other high-symmetry points in structurally chiral crystals with relevant SOC[235,236], where structural chirality is defined through the absence of rotoinversion symmetries such as mirror or $\mathcal{I}$[26]. Unlike band-inversion Weyl points, Kramers–Weyl points are formed from two Bloch states at a momentum $\mathbf{k}$ that transform in a two-dimensional, double-valued small corep of a chiral little group G_k (REF.[235]). Kramers–Weyl points have since been predicted in $Ag_2Se_{0.3}Te_{0.7}$ (REF.[235]), and have been experimentally investigated in chiral tellurium [ICSD 23062, SG 152 ($P3_121$)] through ARPES[237] and in β-Ag_2Se [ICSD 260148, SG 19 ($P2_12_12_1$)][238] and few-layer chiral tellurium[239] through quantum oscillations. The complete set of single-valued coreps corresponding to weak-SOC variants of Kramers–Weyl points was also recently enumerated[240]. Lastly, Weyl semimetals have emerged as a playground for topological bulk response effects (FIG. 2), with the transition-metal monophosphides TaAs and NbP and the half-Heusler GdPtBi [ICSD 58786, SG 216 ($F\bar{4}3m$)] in an external magnetic field notably providing platforms for the observation of the gravitational anomaly[241,242] and the chiral anomaly[243–250].

Unconventional TSMs and chiral crystals

Following the initial characterization of Dirac and Weyl semimetals, researchers over the past five years have recognized the existence of increasingly exotic variants of unconventional TSMs without analogues in high-energy physics, including closed rings of nodal points — known as nodal lines[251–253] — and nodal points whose $\mathbf{k}\cdot\mathbf{p}$ Hamiltonians do not resemble the dispersion relations of familiar relativistic particles[254,255]. In many 3D nodal-line semimetals, the surface projections of the nodal lines are filled with 2D puddles of topological, flat-band-like drumhead surface states that originate from a π shift in the bulk polarization density (surface-directed Berry phase) between the interior and exterior of the nodal line[251,252]. Nodal-line TSMs with drumhead surface states have been proposed in an overwhelming number of solid-state materials[195,251–253,256–258], and have been experimentally investigated in numerous compounds, including Ca_3P_2 in a novel structural phase through X-ray diffraction[259]; ZrSiS [ICSD 15569, SG 129 ($P4/nmm$)][260,261], CaAgAs [ICSD 10017, SG 189 ($P\bar{6}2m$)][262], $PbTaSe_2$ [ICSD 74704, SG 187 ($P\bar{6}m2$)][263], and ZrB_2 [ICSD 615755, SG 191 ($P6/mmm$)][264] through ARPES; $NbAs_2$ [ICSD 81218, SG 12 ($C2/m$)][265] through optical conductivity measurements; and ZrSiSe [ICSD 15571, SG 129 ($P4/nmm$)] through quasiparticle interference in STM[266].

Next, beginning with the prediction of eightfold double Dirac points in materials including Bi_2AuO_5 [ICSD 82092, SG 130 ($P4/ncc$)][254] and $CuBi_2O_4$ [ICSD 56390, SG 130 ($P4/ncc$)][255] (although the latter would prove to be a Mott insulator owing to interactions[267,268]), researchers identified unconventional nodal point semimetals that lie between or beyond the earlier Dirac and Weyl classification schemes (FIG. 5a,b). Examples include the band-inversion, partially dispersing threefold points predicted in θ-TaN [ICSD 76455, SG 187 ($P\bar{6}m2$)][269] and in the WC family [ICSD 672362, SG 187 ($P\bar{6}m2$)][270,271] and confirmed through ARPES in MoP [ICSD 644091, SG 187 ($P\bar{6}m2$)][272] and WC[273], the coexisting Dirac and Weyl points predicted in the SrHgPb family [ICSD 602710, SG 186 ($P6_3mc$)][274], and the achiral sixfold fermions observed in $PdSb_2$ [ICSD 77109, SG 205 ($Pa\bar{3}$)] through ARPES experiments[275]. In the abovementioned band-inversion threefold point and mixed Dirac–Weyl TSMs, the nontrivial bulk stable topology and topological surface states originate from a combination of band inversion and chiral-fermion (Weyl-point) descent relations, but are not directly related to the bulk threefold and Dirac points themselves[276]. High-symmetry-point sixfold fermions were also predicted to lie near E_F in CoSi [ICSD 260982, SG 198 ($P2_13$)] and AlPt [ICSD 672522, SG 198 ($P2_13$)][255].

Most notably, recent advances in TSMs have come from identifying conventional and unconventional nodal degeneracies in structurally chiral crystals. First, the authors of REF.[235] demonstrated that all point-like degeneracies in structurally chiral crystals necessarily exhibit nontrivial chiral charges, implying that all nodal-point TSMs with structurally chiral SGs are topologically chiral TSMs (semimetallic phases in which bulk Fermi pockets carry nontrivial chiral charges). This led to the ab initio prediction[277,278] that members of the RhSi (B20) chiral crystal family [ICSD 79233, SG 198 ($P2_13$)] — including the abovementioned examples of CoSi and AlPt[255] — host topological Fermi arcs that span the surface BZ and link the projections of essential, high-symmetry-point, unconventional, chiral fermions (FIG. 5c). Zone-spanning surface Fermi arcs were subsequently observed in ARPES measurements of CoSi[279–281] (FIG. 5d) and AlPt[282], and through quasiparticle interference in STM probes of CoSi[283]. Following those experiments, BZ-spanning topological surface Fermi arcs were observed through ARPES in numerous other topological chiral crystals, including PdGa [ICSD 261111, SG 198 ($P2_13$)][284] (FIG. 5e), PtGa [ICSD 635132, SG 198 ($P2_13$)][285], RhSn [ICSD 650381, SG 198 ($P2_13$)][286] and PdBiSe [ICSD 616956, SG 198 ($P2_13$)][287]. Lastly, chiral TSM phases in structurally chiral crystals have also been recognized as ideal systems for experimentally probing topological response effects. Structurally chiral TSMs have been theoretically proposed as platforms for realizing topological superconductivity[288,289], and recent experiments have demonstrated a nearly-quantized circular photogalvanic effect[235,277,290–292] in RhSi[293] and CoSi[294]; quantum-oscillation signatures of topological superconductivity in AuBe [ICSD 58396, SG 198 ($P2_13$)][295]; and

high-efficiency and enantioselective catalysis in AlPt, PtGa and PdGa[11,12].

Topological quantum chemistry and symmetry-based indicators

As discussed in the subsection 'Diagnosing band topology', if a set of bands is not Wannierizable, then the bands are either stable or fragile topological. In 2017, researchers exploited this reasoning to formulate the theory of TQC[31,32,58,85–87] as a means of predicting the **k**-space topology of a material from its **r**-space chemistry. In TQC, the bands of (obstructed) atomic limits transform in band coreps that are induced from Wannier orbitals that in turn transform in the coreps of the site-symmetry groups {$G\mathbf{q}$} of a crystal. Specifically, each $G\mathbf{q}$ is defined as the group of symmetries that return the point **q** to itself in the same unit cell. TQC is based on the statement that in any SG, the bands of any (obstructed) atomic limit transform in a linear combination of elementary band coreps, defined as the band coreps that cannot be expressed as direct sums of other band coreps[32,87,296,297]. The elementary band coreps of all 230 nonmagnetic SGs were made available for TQC through the BANDREP tool on the Bilbao Crystallographic Server[31,32]. Importantly, each elementary band corep is not just a collection of small coreps at each high-symmetry **k** point, but also includes the (nested) Berry phases that encode the relative positions of the underlying atomic orbitals[58,59,68,85]. Because the bands that transform in elementary band coreps span the set of Wannierizable bands in each SG, any energetically isolated set of bands that does not transform in a band corep must be stable or fragile topological.

The presence of some stable topological phases, such as Chern insulators and 3D TIs, can be inferred from the symmetry eigenvalues of the occupied bands[41,113,114]. By exploiting an enumeration of (obstructed) atomic limits equivalent to TQC, a method was developed to identify the linearly independent SI groups (such as $\mathbb{Z}_4 \times \mathbb{Z}_2^3$) and SI formulas (such as the Fu–Kane parity criterion[41]) for stable topology in each SG[115,117,118,121]. In this method, the SIs of an SG are determined by solving a set of Diophantine equations using the Smith-normal form[298] of the matrix of small corep multiplicities of each elementary band corep[299–302]. The procedure returns a set of SI topological bands that cannot be expressed as integer-valued linear combinations of elementary band coreps, and are hence stable topological. From the SI

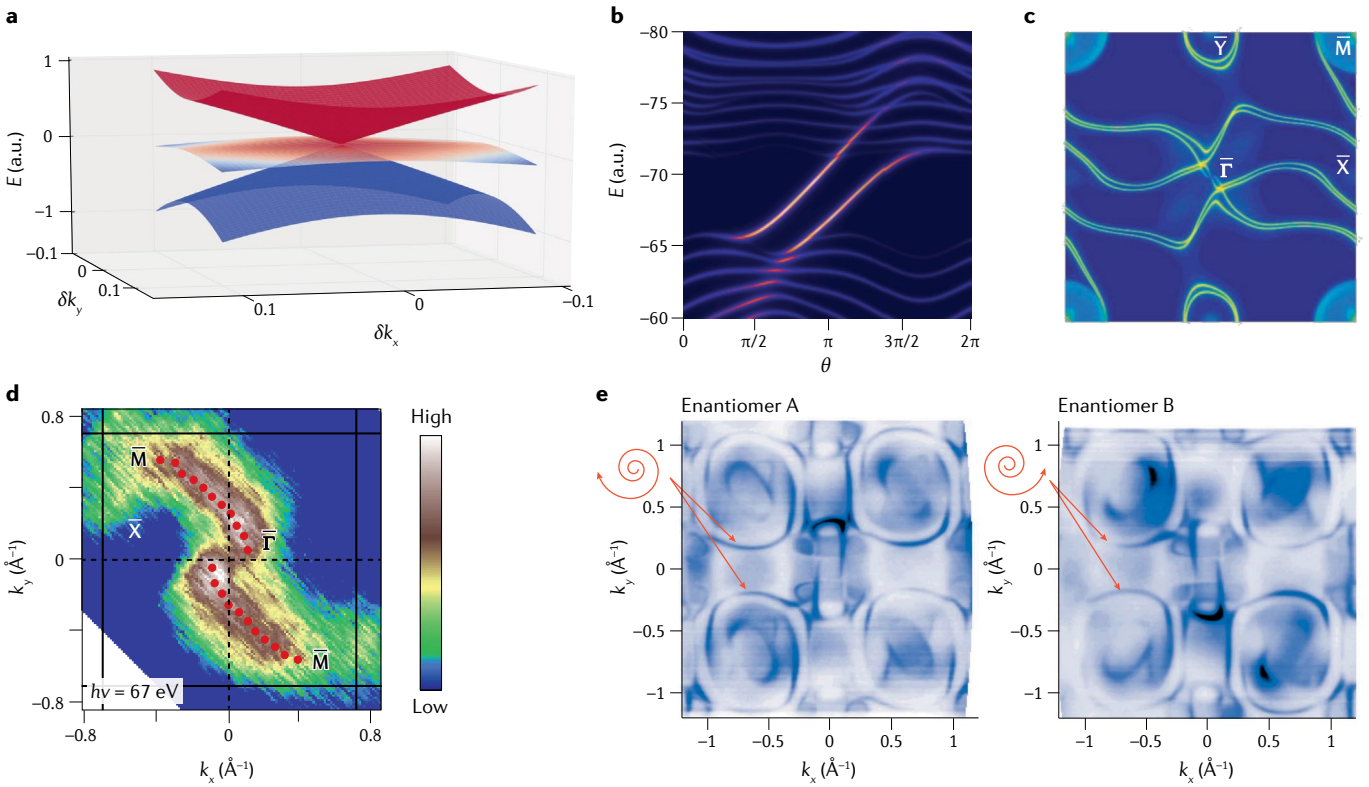

Fig. 5 | **Chiral topological semimetal phases in structurally chiral crystals. a** | The dispersion relation of a spin-1 chiral fermion. Because the nodal point of the spin-1 fermion is threefold-degenerate, the spin-1 fermion is an example of an unconventional quasiparticle beyond condensed-matter realizations of Dirac and Weyl fermions[254,255], which correspond to fourfold and twofold nodal degeneracies with linear dispersion, respectively. **b** | Surface Fermi arcs of a tight-binding model of a chiral topological semimetal with spin-1 fermions at the Fermi energy. Two surface Fermi arcs with positive slopes cross the bulk gap, indicating that the spin-1 fermions carry the chiral charges ±2. **c** | Dramatically long topological Fermi arcs spanning the 2D Brillouin zone of the surface of a 3D topological chiral crystal in the RhSi (B20) family of materials [ICSD 79233, SG 198 ($P2_13$)], calculated from first principles[235,277,278]. **d** | Angle-resolved photoemission spectroscopy (ARPES) data confirming the presence of zone-spanning topological surface Fermi arcs in B20-CoSi [ICSD 260982, SG 198 ($P2_13$)][279–281]. **e** | ARPES data demonstrating the dependence of the helicity of the surface Fermi arcs on sample structural chirality in B20-PdGa [ICSD 261111, SG 198 ($P2_13$)]. Panels **a** and **b** adapted with permission from REF.[255], AAAS. Panel **c** reprinted with permission from REF.[277], APS. Panel **d** reprinted with permission from REF.[279], APS Physics. Panel **e** reprinted with permission from REF.[284], AAAS.

topological bands, one may then obtain the SI groups and formulas of each SG in an arbitrary basis in which nontrivial SIs generically indicate superpositions of recognizable TIs and TCIs. The SI groups for the 230 SGs were computed in REF.[117]. Shortly afterwards, equivalent, intuitive bases and the associated anomalous boundary states were determined for each stable SI formula[118–121]. As we discuss in the section 'Higher-order TCIs and TSMs', the SI formulas in REFS[117,119,120] revealed the existence of numerous symmetry-indicated HOTI phases, which included the HOTIs first identified in REFS[67,116]. SIs for fragile topological bands[58,85,88,89] have also been introduced[90,91]. Most recently, the SIs of the 230 nonmagnetic SGs were used to generate large databases of topological materials[15,16,122–124].

Higher-order TCIs and TSMs

In 2015, a revolution in topological materials was initiated by the introduction of a model of a 2D quadrupole insulator with gapped 1D edges and anomalous, fractionally-charged 0D corner states[65] (FIG. 6a). Though earlier works had demonstrated that d-D topological phases could host $(d-2)$-D topological modes[254,303–307], the quadrupole insulator model was the first system in which the presence of $(d-2)$-D boundary states was recognized to be an intrinsic consequence of the d-D bulk band topology. Shortly afterwards, several works[66,67,78,116,118,169,308–310] demonstrated the existence of 3D HOTI phases with intrinsic 1D chiral or helical hinge states (FIG. 6b).

The complete SIs of the 230 nonmagnetic SGs were computed in REFS[117,119,120], initially on a parallel research track to the HOTI models introduced in REFS[65,66]. However, researchers uncovered instances of models and real materials with trivial Fu–Kane parity[41] and rotation-indicated TCI indices[114], but whose occupied bands exhibited nontrivial stable SIs[117,119,120]. It was quickly recognized that the new TCI phases generically exhibited combinations of 2D surface states and 1D hinge modes, and included the HOTI phases proposed in REFS[67,118]. The simplest symmetry-indicated HOTI — a 'doubled' 3D TI — occurs in SG 2 ($P\bar{1}$), and is formed from two superposed copies of an $\mathcal{I}$- and $\mathcal{T}$-symmetric 3D TI (FIG. 6b). From a physical perspective, doubled 3D TI phases occur in centrosymmetric materials with a double band inversion at the same TRIM point[67,69]. This realization motivated the promotion of the $\mathbb{Z}_2$ Fu–Kane parity criterion to a $\mathbb{Z}_4$ index for $\mathcal{I}$- and $\mathcal{T}$-symmetric insulators[67,69,117,119,120], coinciding with the $\mathbb{Z}_4$-valued SI Z_4 that results from performing for SG 2 ($P\bar{1}$) the Smith-normal form calculation outlined in the section 'Topological quantum chemistry and symmetry-based indicators'. In a concurrent work, however, it was shown that the fourfold Dirac surface states of the new phase — the $Z_4 = 2$ doubled 3D TI — are unstable, because the fourfold surface Dirac cones are not protected by the wallpaper group symmetries of a crystal in SG 2 ($P\bar{1}$)[78]. In rapid succession, several groups determined that when a doubled 3D TI is cut in an $\mathcal{I}$-symmetric geometry, the mass of the fourfold surface Dirac cone has opposite signs on surfaces with $\mathcal{I}$-related Miller indices, resulting in a network of sample-encircling, intrinsic, helical hinge modes[116,119,120] (FIG. 6b).

Using the topological invariants introduced in REF.[67], a HOTI phase protected by $\mathcal{T}$ and fourfold rotation symmetry[118,169] was predicted in strained SnTe [ICSD 601065, SG 225 ($Fm\bar{3}m$)]. Shortly afterwards, using SIs, TQC, and reinterpreting earlier data from STM[132] and

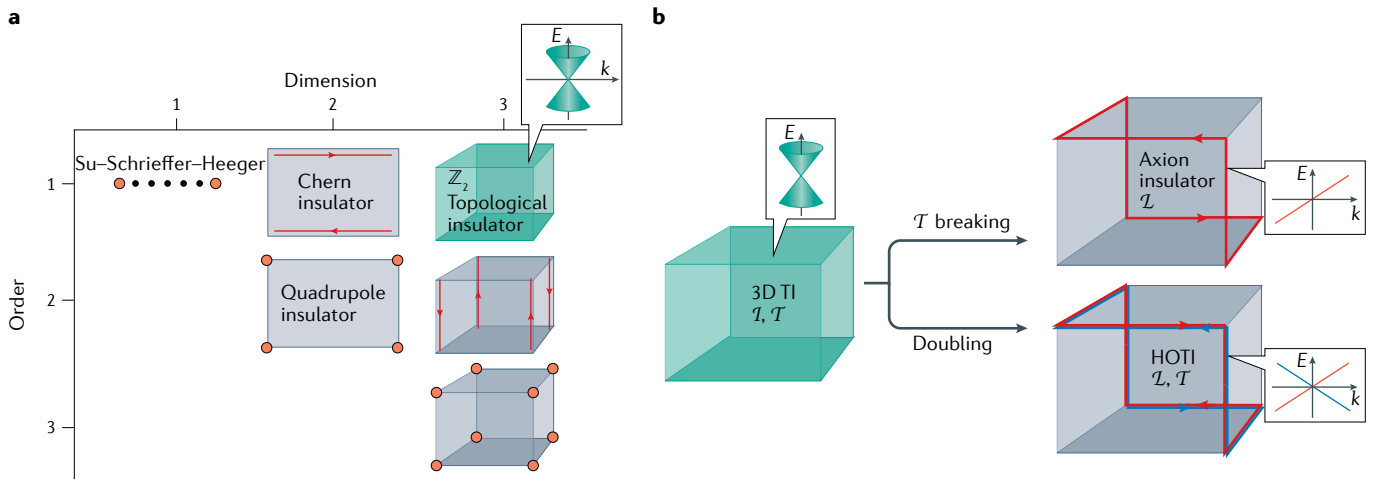

Fig. 6 | **Higher-order topological crystalline insulators. a** | The classification of nth-order topological insulators (TIs) and topological crystalline insulators (TCIs) in d dimensions[66,67]. In this classification scheme, dth-order TCIs in d dimensions exhibit anomalous boundary charge and spin that manifest as midgap 0D states near the chiral-symmetric limit. Hence, dth-order TCIs in d dimensions — like the 2D quantized quadrupole insulator[65] — are necessarily fragile topological or obstructed atomic limits[59,68,69]. We emphasize that in most 3D solid-state TCIs with 1D hinge states, like SnTe[67] and bismuth crystals[116,407], there also exist anomalous 2D surface states[59,78,119,120,169]. Nevertheless, whether a material is interpreted to be a TCI or a higher-order TCI (HOTI), the classification of the bulk topology can unambiguously be determined through symmetry-based indicators[115,117–121,299–302], (nested) Wilson loops[57–59,65–69,71–78], and layer constructions[119,408,409]. **b** | The simplest 3D HOTIs can be constructed from 3D TIs with inversion ($\mathcal{I}$) and time-reversal ($\mathcal{T}$) symmetry. First, applying $\mathcal{I}$-symmetric magnetism to an $\mathcal{I}$- and $\mathcal{T}$-symmetric 3D TI gaps the twofold Dirac-cone surface states to reveal the intrinsic chiral hinge modes of a magnetic axion insulator[41,59,69,101,104,143,305,308,324–329,333,334]. Alternatively, superposing two $\mathcal{I}$- and $\mathcal{T}$-symmetric 3D TIs results in a non-axionic 3D HOTI phase in which unstable fourfold surface Dirac cones[69,78] gap into a network of intrinsic helical hinge modes[116,117,119,120].

superconducting transport experiments[311], the existence of a $Z_4 = 2$ HOTI phase with helical 1D channels was theoretically predicted and experimentally confirmed in rhombohedral bismuth crystals [ICSD 64703, SG 166 ($R\bar{3}m$)][116]. Although subsequent works[312,313] have provided alternative interpretations for the STM data, bismuth-like supercurrent oscillations have since been observed in other candidate HOTIs[69], including $MoTe_2$ [ICSD 14349, SG 11 ($P2_1/m$)][314] and WTe_2 [ICSD 14348, SG 31 ($Pmn2_1$)][315–317]. Additionally, hinge-state-like 1D channels have been observed in STM probes of $MoTe_2$ samples with coexisting structural orders[318] and in spectroscopic probes[319–321] of the candidate HOTI BiBr [ICSD 1560, SG 12 ($C2/m$)][124,322,323]. Notably, whereas the HOTI phases in bismuth, β-$MoTe_2$ and BiBr are indicated by $Z_4 = 2$[124,322,323], the HOTI phases in noncentrosymmetric γ-$MoTe_2$ and γ-WTe_2 can only be diagnosed by computing a nested Wilson loop[69].

The discovery of HOTIs also resolved previous ambiguities in the characterization of magnetically doped 3D TIs. It had been known since the identification of the first 3D TIs that breaking $\mathcal{T}$ symmetry can drive a 3D TI into an axion insulator phase with gapped bulk and surface states and gapless (chiral) hinge modes[41,104,143,305,324–329]. Axion insulators inherit their name from early work by Frank Wilczek[330] and Edward Witten[331] on high-energy field theories that exhibit axion electrodynamics as a consequence of incorporating magnetic monopoles. Signatures of axion electrodynamics were recently observed in terahertz spectroscopy probes of the 3D TI Bi_2Se_3 [ICSD 42545, SG 166 ($R\bar{3}m$)] in an external magnetic field[332]. Through a combination of magnetic SIs[117,299,300,308,333] and boundary-state calculations[59,69,329,334] of magnetically gapped, $\mathcal{I}$-symmetric TIs, it was revealed that axion insulators are in fact magnetic HOTIs with intrinsic hinge states (FIG. 6b). Whereas the bulk topology of an $\mathcal{I}$-symmetric axion insulator may be inferred from the Fu–Kane parity formula[324,325,327], all of the surface states and Wilson loops are generically gapped in an axion insulator with only bulk $\mathcal{I}$ symmetry, and the nontrivial bulk topology manifests as chiral spectral flow in the hinge and nested Wilson spectra[59]. Notably, there also exist axion insulator phases protected by bulk symmetries other than $\mathcal{I}$ — such the product of twofold rotation and $\mathcal{T}$ — in which the bulk topology cannot be diagnosed from SIs, and is only indicated by (nested) Wilson loop winding[59,101,334]. Axion insulator phases have been proposed in Sm-doped Bi_2Se_3 (REF.[335]) and $MnBi_2Te_4$ [ICSD 425966, SG 166 ($R\bar{3}m$)][336,337], and experimental signatures of axion insulators have been observed in transport and ARPES probes of Cr- and V-doped $(Bi,Sb)_2Te_3$ heterostructures[338,339] and in $MnBi_2Te_4$ (REFS[340,341]).

Lastly, by using TQC to re-express the original quadrupole insulator model as a magnetic obstructed atomic limit formed from s–d-orbital hybridization, researchers discovered the existence of solid-state higher-order TSM phases with flat-band-like hinge states[68]. In Dirac higher-order TSM phases, there may or may not also exist topologically trivial Fermi-arc surface states; nevertheless, Dirac higher-order TSM phases universally host intrinsic hinge states as a topological consequence of their bulk Dirac points[68,342]. Dirac higher-order TSM phases have since been predicted to occur in nearly all previously identified band-inversion Dirac semimetals[68], and signatures of hinge states were recently observed in supercurrent oscillation experiments on the established Dirac semimetal Cd_3As_2 [ICSD 609930, SG 137 ($P4_2/nmc$)][343]. Most recently, researchers have also predicted the existence of nodal-line[69,344], Weyl[345] and sixfold-point[82] higher-order TSM phases. In higher-order TSM materials like Cd_3As_2, the bulk nodal degeneracies are equivalent to the quantum critical points between 2D insulators that differ by a quantized nested Berry phase, implying that the flat-band-like hinge states originate from higher-order-topological descent relations[68,69,342,345].

The Topological Materials Database

TQC[31,32,58,85–87] and related methods[115,117,119,120] have changed the mindset of the topological materials community, shifting the focus in materials discovery from human intuition to algorithmic materials prediction. In particular, TQC has allowed the methods first introduced in REFS[193–195,197,254,255] for predicting enforced semimetals and in REFS[41,114] for predicting TIs and TCIs to be implemented for high-throughput topological materials discovery. Exploiting the complete enumeration of symmetry-indicated TIs, TCIs, TSMs, HOTIs, higher-order TSM phases, and atomic limits (elementary band coreps) developed over the past decade, researchers over the past two years have successfully performed large-scale searches for topological materials. Utilizing the resources of the ICSD[13,14] and the Materials Project[346], researchers applied the theories of TQC[31,32,58,85–87] and SIs[115,117,119,120] to the automated output of thousands of first-principles investigations of nonmagnetic chemical compounds, resulting in massive databases of stoichiometric topological materials[15,122–124]. Specifically, density functional theory[347,348] calculations were performed on about 25,000[15], about 40,000[122] and about 20,000[123] of the 193,426 material structures entered in the ICSD — after applying filters to remove alloys, entries with large numbers of atoms per unit cell and materials containing heavy elements with f electrons at E_F. Around 8,000 ICSD entries were identified as stable TIs, TCIs and TSMs at E_F (intrinsic electronic filling). Most recently, an exhaustive high-throughput topological analysis of all of the stoichiometric materials in the ICSD was completed[16]. In this section, we review the methodology and results of this analysis[16], which are freely accessible on the Topological Materials Database.

When the analysis in REF.[16] was performed, the ICSD contained 193,426 entries, including multiple entries for the same material with varying structural parameters obtained in different experimental works. First, the researchers excluded materials that were not close to the stoichiometric limit and entries with incorrect structure files (for example, files missing atoms present in the chemical formula), and then rounded nearly-stoichiometric materials to have integer-valued atomic occupancies. This process reduced the initial 193,426 ICSD entries down to 96,196 stoichiometric entries with processable structure files. The researchers

then performed high-throughput density functional theory using the Vienna ab initio Simulation Package (VASP)[349,350] on these 96,196 ICSD entries, both with and without incorporating the effects of SOC. The high-throughput calculations resulted in convergent electronic structures for 73,234 ICSD entries in the presence of SOC. To analyse the resulting electronic structures with TQC, the researchers applied the VASP2Trace tool[351] that was previously implemented for the analysis in REF.[15], and then wrote a new implementation of the Check Topological Mat. tool on the Bilbao Crystallographic Server. The VASP2Trace program[351] specifically outputs the small coreps that correspond to the Bloch states in each band at each **k** point, and Check Topological Mat. determines whether an energy gap is permitted at a given electronic filling, and determines the stable and fragile SIs of all energetically isolated groups of bands. After using VASP2Trace[351] and Check Topological Mat. to analyse the 73,234 ICSD entries with convergent band-structure calculations, it was determined that the data contained 38,298 unique materials, defined such that two ICSD entries with the same chemical formulas, crystal structures, and bulk topology at E_F were associated to the same unique material. The computational calculations performed to generate the Topological Materials Database required 22.60 million central-processing-unit (CPU) hours.

For each ICSD entry in the Topological Materials Database, the topology is characterized using TQC from two perspectives: cumulative band topology and energetically isolated topological bands. In the first approach, given the number of electrons in each unit cell, the topology at E_F is calculated using TQC and SIs, and is then sorted into one of the five broad categories defined in REF.[15]. First, if the occupied bands of the material can be expressed as a linear combination of elementary band coreps, the material is classified as LCEBR. LCEBR materials, in general, are either trivial or fragile topological, or host non-symmetry-indicated stable topology; in REF.[16], the authors did not observe any materials for which the entire valence manifold was fragile topological. Next, if the symmetry eigenvalues of the occupied bands imply the existence of a TSM phase, the material is labelled as an enforced semimetal with Fermi degeneracy if the bulk is a high-symmetry-point TSM, and is labelled as an enforced semimetal (ES) if the bulk is a high-symmetry-line or plane TSM. Last, if a gap is permitted at E_F and the bulk exhibits nontrivial stable SIs, the occupied bands are either classified as a split elementary band corep (SEBR), or as "not equal to a linear combination" (NLC), depending on whether the occupied bands can or cannot be expressed as linear combinations of pieces (disconnected branches) of elementary band coreps[86,87]. Of the 38,298 unique materials, 18,133 (47.35%) were LCEBR, 14,037 (36.65%) were enforced TSMs at E_F, and 6,128 (16.00%) were TIs and TCIs with nontrivial stable SIs. These results surprisingly implied that 52.65% of the known stoichiometric 3D materials are symmetry-indicated TIs, TCIs or TSMs at intrinsic filling (E_F). Notably, this is considerably higher than the percentage of topological stoichiometric 2D materials, which has been computed to lie within the range of a few to 20%[352–355].

Unlike in previous high-throughput topological analyses[15,122–124], the version of Check Topological Mat. implemented for REF.[16] allowed researchers to analyse the symmetry-indicated stable and fragile topology of energetically isolated bands away from E_F. This enabled the authors of REF.[16] to employ a second approach towards topological materials characterization. For each ICSD entry in the Topological Materials Database, the researchers additionally calculated the stable and fragile topology of each set of isolated bands in the energy spectrum as defined by band connectivity through TQC[31,32,85–87]. Discarding bands from core-shell atomic orbitals, it was discovered that among all of the isolated bands in all of the 38,298 analysed unique materials, 0.37% of bands are fragile topological, 62.05% of bands — nearly two-thirds — are stable topological, and an overwhelming 87.99% of known stoichiometric materials contain at least one stable or fragile topological band. These numbers are all the more shocking when one considers that many of the unique materials in the Topological Materials Database respect the symmetries of one of the 117 noncentrosymmetric, nonmagnetic SGs in which stable topology cannot be determined by SIs[119,120]. Indeed, the analysis in REF.[16] has revealed that band topology is one of the most fundamental and generic properties of solid-state materials.

Each of the three research groups that performed the high-throughput searches for topological materials[15,16,122–124] implemented a website enabling users to access the resulting data. In addition to the abovementioned Topological Materials Database implemented for REFS[15,16], high-throughput first-principles topological material calculations can be accessed on the Catalogue of Topological Materials created for REF.[122] and the Topological Materials Arsenal created for REFS[123,124]. All three websites allow users to search for materials by SG and chemical formula, with further functionality and more complete topological characterizations being dependent on the particular website. The Topological Materials Database and the Catalogue of Topological Materials, in particular, allow users to perform more advanced queries, including searches restricted to materials with specific gap sizes and stable SIs. The Topological Materials Database additionally provides users with the stable and fragile topological classification of energetically isolated bands away from E_F. In FIG. 7 we show examples of materials in the Topological Materials Database identified in REF.[16] as hosting novel topological properties.

Conclusion and future directions

In this Review, we have followed the discovery of solid-state topological materials from the first theoretical proposals of $\mathcal{T}$-symmetric TIs to the recent identification of tens of thousands of candidate TIs, TCIs and TSMs via high-throughput searches. Despite the recent completion of nonmagnetic solid-state group theory[31,32,85–87,117,119,120], and the complete analysis of the stoichiometric materials in the ICSD performed in REF.[16], there remain many unexplored directions for topological materials discovery. First, the methods used to identify topological materials in REFS[15,16,122–124,300] can be applied only to materials with nontrivial stable

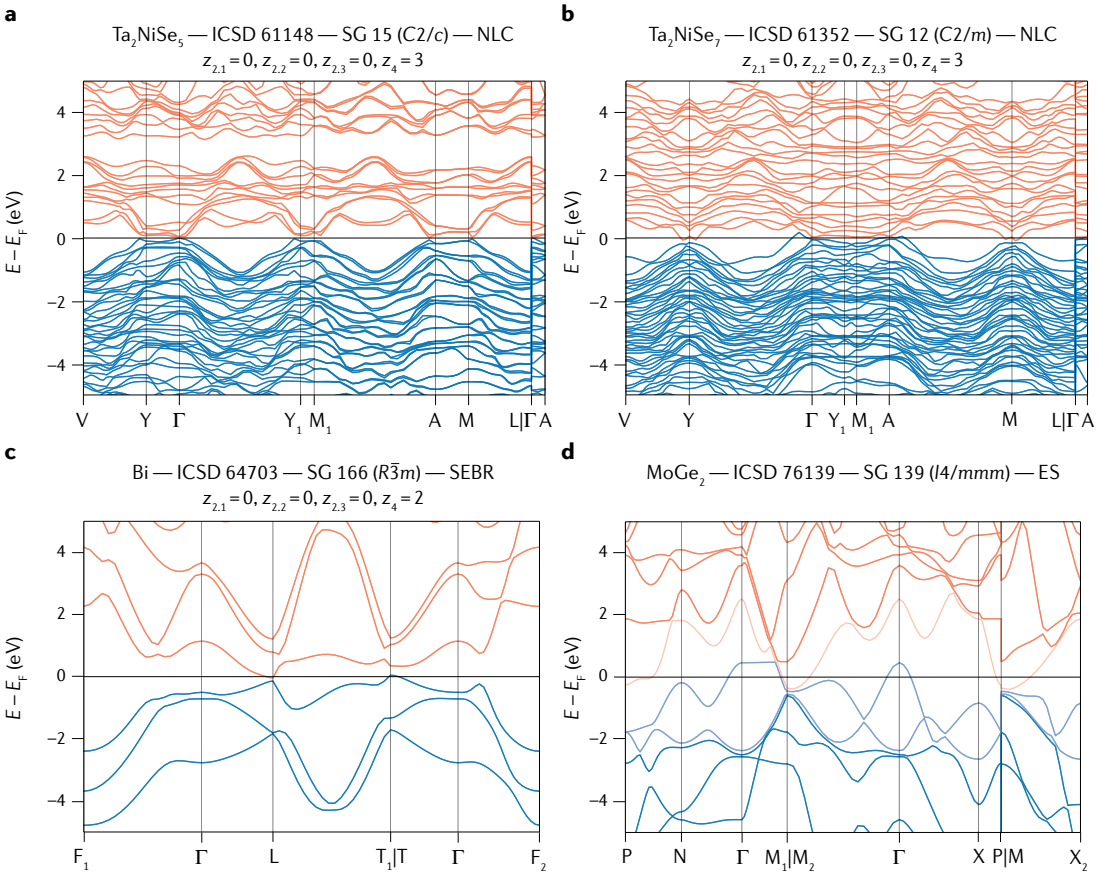

Fig. 7 | **Representative materials with novel topological properties identified in the Topological Materials Database.** For each material in this figure, we have provided the Inorganic Crystal Structure Database (ICSD) accession code and the number and standard-setting symbol of the crystallographic space group (SG) of the material[27]. For materials that are topological insulators (TIs) or topological crystalline insulators (TCIs) at intrinsic electronic filling, we additionally provide the cumulative symmetry-based indicators of the gap at the Fermi energy (E_F) in the notation established in REF.[119]. **a** | The layered transition-metal chalcogenide Ta_2NiSe_5 [ICSD 61148, SG 15 (*C*2/*c*)] was measured in transport experiments to be an excitonic insulator[410,411]; in REF.[16], the narrow-gap semiconducting state of Ta_2NiSe_5 was revealed to be a $Z_4 = 3$ 3D TI. Because its occupied bands cannot be expressed as a linear combination of disconnected branches of elementary band corepresentations (coreps), Ta_2NiSe_5 is classified as 'not equal to a linear combination' (NLC). **b** | The closely related quasi-1D transition-metal chalcogenide Ta_2NiSe_7 [ICSD 61352, SG 12 (*C*2/*m*)], which conversely exhibits a charge-density-wave instability[412], was found in REF.[16] also to be a $Z_4 = 3$, NLC-classified 3D TI in its normal state. **c** | Bi [ICSD 64703, SG 166 ($R\bar{3}m$)] was previously recognized to be a $Z_4 = 2$ helical higher-order TCI[116]; in REF.[16], it was discovered that the bands below E_F in rhombohedral bismuth also exhibit stable topology. Because the occupied bands of bismuth can be expressed as a linear combination of disconnected pieces of elementary band coreps, the bulk topology of bismuth originates from a split elementary band corep (SEBR). **d** | $MoGe_2$ [ICSD 76139, SG 139 (*I*4/*mmm*)] was identified in REF.[16] as a higher-order topological enforced semimetal (ES) with fourfold Dirac points near E_F in which the two conduction and four valence bands closest to E_F (doubly-degenerate light red and light blue bands) are, as a set, fragile topological.

and fragile SIs, which are largely centrosymmetric. However, the ICSD[13,14] contains thousands of non-centrosymmetric compounds. Because it has been discovered[16] that 87.99% of the stoichiometric materials in the ICSD contain topological bands when only SIs are taken into account, there likely exist thousands of as-yet-unidentified noncentrosymmetric TIs, TCIs, and TSMs. Furthermore, whereas the complete stable SIs of magnetic and nonmagnetic TIs, TCIs and TSMs have been computed[117,119–121,299,300,333], the magnetic fragile SIs remain an outstanding problem. One route towards the discovery of topological materials beyond SIs involves developing a high-throughput protocol based on carefully selected Wilson loop calculations; several promising early efforts in this direction have recently been completed[111,112]. Additionally, despite recent early efforts[59,68,69,76–78], there remain several 3D TCI phases without SIs that have been identified through layer constructions and surface state calculations[119,299], but do not yet have accompanying bulk ((nested) Wilson loop) topological invariants.

Second, TQC was extended this past year to crystals with commensurate magnetism to construct the theory of magnetic TQC[299]. The formulation of magnetic TQC required the intermediate computation of the magnetic small coreps and elementary band coreps, completing the century-old problem of enumerating irreducible coreps in solid-state group theory[356–358]. Through

magnetic TQC, the complete SI groups and formulas of spinful band topology in all 1,651 magnetic and nonmagnetic SGs were determined[299], subsuming an earlier calculation of the magnetic SI groups[333], and leading to the discovery of several novel variants of magnetic HOTIs. Magnetic TQC was most recently employed to perform a high-throughput search for magnetic topological materials[300], resulting in the identification of over 100 magnetic TIs, TCIs, and TSMs among the approximately 500 magnetic materials on the Bilbao Crystallographic Server with experimentally measured magnetic SGs[359–362]. Structurally chiral magnetic TSM phases were also recently proposed in chiral crystals with commensurate magnetic ordering, including Mn_3IrSi [ICSD 151748, SG 198 ($P2_13$)][363]. However, despite these results, and the recent experimental identification of novel magnetic TCIs[338–341,364] and TSMs[365–367], the number of materials whose commensurate magnetic structures have been measured through neutron diffraction and matched with magnetic SGs remains several orders of magnitude smaller than the number of nonmagnetic materials with measured crystal structures and SGs. It is our hope that the recent successes of magnetic TQC and magnetic SIs will encourage experimentalists and computational materials scientists to analyse larger numbers of magnetic structures using the magnetic SG classification of magnetic crystalline solids[27]. This symmetry analysis would facilitate future theoretical and experimental investigations of materials with linked magnetic and topological order, both at the mean-field level of magnetic TQC[299] and beyond.

As a third future direction, many of the compounds in the ICSD feature unreported structural phases or chemical complexities beyond the simple descriptions provided in their structure files. A hybrid methodology combining the intuition of trained chemists with high-throughput calculations of topological electronic structures[15,16,122–124] could facilitate the development of advanced alloyed or heterostructure topological materials. The engineering of topological heterostructure and few-layer devices in particular has emerged as a promising direction for future studies. For example, researchers have experimentally demonstrated an electronically switchable photocurrent response in the 2D TI WTe_2[368] and cuprate-like superconductivity in twisted bilayer graphene[369–371]. Most intriguingly, recent theoretical[59,93,96–98,372–375] and experimental[376–383] studies have revealed a relationship between the superconductivity and other interacting phases in twisted bilayer graphene and both fragile and higher-order topology. Further investigations into few-layer topological device engineering may therefore provide insight into some of the largest outstanding problems in solid-state physics, such as the mechanism of superconductivity in the high-temperature cuprate superconductors[384].

Finally, although this Review is largely focused on noninteracting topological phases with crystal symmetry, an emerging future direction in topological materials involves the experimental manipulation of charge-density-wave and spin-density-wave phases in solid-state materials. For example, recent theoretical and experimental investigations have provided evidence that structurally chiral, quasi-1D $(TaSe_4)_2I$ crystals [ICSD 35190, SG 97 ($I422$)] are Weyl semimetals that become gapped by an incommensurate charge-density wave[385]. In earlier works, Weyl-charge-density-wave insulators were proposed to be correlated axion insulators[386–388], though recent investigations have revealed that the axionic response of Weyl-charge-density-waves is captured by mean-field theory[389–391]. The prediction[385] of a Weyl-charge-density-wave phase in $(TaSe_4)_2I$ was recently confirmed through ARPES measurements of high-temperature Weyl points[392] and transport experiments demonstrating axionic response effects in the low-temperature charge-density-wave phase[393]. As discussed earlier in this Review, axion insulators have recently been recognized to be HOTIs; additionally, recent theoretical investigations[394] of the charge-density-wave phase in 1T-TaS_2 [ICSD 52115, SG 164 ($P\bar{3}m1$)][395] have demonstrated the presence of higher-order topological corner states. $\mathcal{T}$-symmetric TSM-charge-density-waves are therefore likely to provide a promising platform for elucidating and exploring novel response effects in helical TCIs and HOTIs, phases of matter that owe their existence to the interplay of symmetry and topology in solid-state materials.

Published online 1 November 2021

1. Kane, C. L. & Mele, E. J. Quantum spin Hall effect in graphene. *Phys. Rev. Lett.* **95**, 226801 (2005).
2. Kane, C. L. & Mele, E. J. Z_2 topological order and the quantum spin Hall effect. *Phys. Rev. Lett.* **95**, 146802 (2005).
3. Bernevig, B. A., Hughes, T. L. & Zhang, S.-C. Quantum spin Hall effect and topological phase transition in HgTe quantum wells. *Science* **314**, 1757–1761 (2006).
4. Kitaev, A. Fault-tolerant quantum computation by anyons. *Ann. Phys.* **303**, 2–30 (2003).
5. Kitaev, A. Anyons in an exactly solved model and beyond. *Ann. Phys.* **321**, 2–111 (2006).
6. Fu, L. & Kane, C. L. Superconducting proximity effect and Majorana fermions at the surface of a topological insulator. *Phys. Rev. Lett.* **100**, 096407 (2008).
7. Mellnik, A. R. et al. Spin-transfer torque generated by a topological insulator. *Nature* **511**, 449–451 (2014).
8. Khang, N. H. D., Ueda, Y. & Hai, P. N. A conductive topological insulator with large spin Hall effect for ultralow power spin–orbit torque switching. *Nat. Mater.* **17**, 808–813 (2018).
9. Pesin, D. & MacDonald, A. H. Spintronics and pseudospintronics in graphene and topological insulators. *Nat. Mater.* **11**, 409–416 (2012).
10. Rajamathi, C. R. et al. Weyl semimetals as hydrogen evolution catalysts. *Adv. Mater.* **29**, 1606202 (2017).
11. Yang, Q. et al. Topological engineering of Pt-group-metal-based chiral crystals toward high-efficiency hydrogen evolution catalysts. *Adv. Mater.* **32**, 1908518 (2020).
12. Prinz, J., Gröning, O., Brune, H. & Widmer, R. Highly enantioselective adsorption of small prochiral molecules on a chiral intermetallic compound. *Angew. Chem.* **127**, 3974–3978 (2015).
13. Bergerhoff, G., Hundt, R., Sievers, R. & Brown, I. D. The inorganic crystal structure data base. *J. Chem. Inf. Computer Sci.* **23**, 66–69 (1983).
14. Allen, F. H. & Shields, G. P. *Crystallographic Databases and Knowledge Bases in Materials Design* 291–302 (Springer, 1999).
15. Vergniory, M. G. et al. A complete catalogue of high-quality topological materials. *Nature* **566**, 480–485 (2019).
16. Vergniory, M. G. et al. All topological bands of all stoichiometric materials. Preprint at *arXiv* https://arxiv.org/abs/2105.09954 (2021).
17. Hasan, M. Z. & Kane, C. L. Colloquium: Topological insulators. *Rev. Mod. Phys.* **82**, 3045–3067 (2010).
18. Marzari, N., Mostofi, A. A., Yates, J. R., Souza, I. & Vanderbilt, D. Maximally localized Wannier functions: theory and applications. *Rev. Mod. Phys.* **84**, 1419–1475 (2012).
19. Armitage, N. P., Mele, E. J. & Vishwanath, A. Weyl and Dirac semimetals in three-dimensional solids. *Rev. Mod. Phys.* **90**, 015001 (2018).
20. Gao, H., Venderbos, J. W., Kim, Y. & Rappe, A. M. Topological semimetals from first principles. *Annu. Rev. Mater. Res.* **49**, 153–183 (2019).
21. Yan, B. & Felser, C. Topological materials: Weyl semimetals. *Annu. Rev. Condens. Matter Phys.* **8**, 337–354 (2017).
22. Nagaosa, N., Morimoto, T. & Tokura, Y. Transport, magnetic and optical properties of Weyl materials. *Nat. Rev. Mater.* **5**, 621–636 (2020).
23. Ashcroft, N. & Mermin, N. *Solid State Physics* (Holt, Rinehart and Winston, 1976).
24. Manna, K., Sun, Y., Muechler, L., Kübler, J. & Felser, C. Heusler, Weyl and Berry. *Nat. Rev. Mater.* **3**, 244–256 (2018).
25. Mermin, N. D. The topological theory of defects in ordered media. *Rev. Mod. Phys.* **51**, 591–648 (1979).

26. Flack, H. Chiral and achiral crystal structures. *Helvetica Chim. Acta* **86**, 905–921 (2003).
27. Bradley, C. & Cracknell, A. *The Mathematical Theory of Symmetry in Solids: Representation Theory for Point Groups and Space Groups* (Clarendon Press, 1972).
28. Conway, J., Burgiel, H. & Goodman-Strauss, C. *The Symmetries of Things*. (AK Peters Series, Taylor & Francis, 2008).
29. Wigner, E. P. in *Nachrichten der Akademie der Wissenschaften in Gottingen. II. Mathematisch-Physikalische Klasse* 546–559 (Springer, 1932).
30. Wigner, E. & Griffin, J. *Group Theory and Its Application to the Quantum Mechanics of Atomic Spectra* (Academic Press, 1959).
31. Bradlyn, B. et al. Topological quantum chemistry. *Nature* **547**, 298–305 (2017).
32. Elcoro, L. et al. Double crystallographic groups and their representations on the Bilbao Crystallographic Server. *J. Appl. Crystallogr* **50**, 1457–1477 (2017).
33. Aroyo, M. I. et al. Bilbao crystallographic server: I. Databases and crystallographic computing programs. *Z. Kristallogr.* **221**, 15–27 (2006).
34. Aroyo, M. I., Kirov, A., Capillas, C., Perez-Mato, J. M. & Wondratschek, H. Bilbao Crystallographic Server. II. Representations of crystallographic point groups and space groups. *Acta Crystallogr. A* **62**, 115–128 (2006).
35. Marzari, N. & Vanderbilt, D. Maximally localized generalized Wannier functions for composite energy bands. *Phys. Rev. B* **56**, 12847–12865 (1997).
36. Resta, R. Macroscopic polarization in crystalline dielectrics: the geometric phase approach. *Rev. Mod. Phys.* **66**, 899–915 (1994).
37. Thouless, D. J., Kohmoto, M., Nightingale, M. P. & den Nijs, M. Quantized Hall conductance in a two-dimensional periodic potential. *Phys. Rev. Lett.* **49**, 405–408 (1982).
38. Thouless, D. J. Quantization of particle transport. *Phys. Rev. B* **27**, 6083–6087 (1983).
39. Thouless, D. J. Wannier functions for magnetic sub-bands. *J. Phys. C* **17**, L325–L327 (1984).
40. Klitzing, K. V., Dorda, G. & Pepper, M. New method for high-accuracy determination of the fine-structure constant based on quantized Hall resistance. *Phys. Rev. Lett.* **45**, 494–497 (1980).
41. Fu, L. & Kane, C. L. Topological insulators with inversion symmetry. *Phys. Rev. B* **76**, 045302 (2007).
42. Chalker, J. T. & Coddington, P. D. Percolation, quantum tunnelling and the integer Hall effect. *J. Phys. C* **21**, 2665–2679 (1988).
43. Lee, D.-H. Network models of quantum percolation and their field-theory representations. *Phys. Rev. B* **50**, 10788–10791 (1994).
44. Ho, C.-M. & Chalker, J. T. Models for the integer quantum Hall effect: The network model, the Dirac equation, and a tight-binding Hamiltonian. *Phys. Rev. B* **54**, 8708–8713 (1996).
45. Pruisken, A. M. Quasi particles in the theory of the integral quantum hall effect: (II). Renormalization of the Hall conductance or instanton angle theta. *Nucl. Phys. B* **290**, 61–86 (1987).
46. Teo, J. C. Y. & Kane, C. L. Critical behavior of a point contact in a quantum spin Hall insulator. *Phys. Rev. B* **79**, 235321 (2009).
47. Fu, L. & Kane, C. L. Topology, delocalization via average symmetry and the symplectic Anderson transition. *Phys. Rev. Lett.* **109**, 246605 (2012).
48. Mong, R. S. K., Bardarson, J. H. & Moore, J. E. Quantum transport and two-parameter scaling at the surface of a weak topological insulator. *Phys. Rev. Lett.* **108**, 076804 (2012).
49. Kimchi, I., Chou, Y.-Z., Nandkishore, R. M. & Radzihovsky, L. Anomalous localization at the boundary of an interacting topological insulator. *Phys. Rev. B* **101**, 035131 (2020).
50. Song, Z.-D. et al. Delocalization transition of a disordered axion insulator. *Phys. Rev. Lett.* **127**, 016602 (2021).
51. Li, H., Jiang, H., Chen, C.-Z. & Xie, X. C. Critical behavior and universal signature of an axion insulator state. *Phys. Rev. Lett.* **126**, 156601 (2021).
52. Cano, J., Elcoro, L., Aroyo, M. I., Bernevig, B. A. & Bradlyn, B. Topology invisible to eigenvalues in obstructed atomic insulators. Preprint at *arXiv* https://arxiv.org/abs/2107.00647 (2021).
53. King-Smith, R. D. & Vanderbilt, D. Theory of polarization of crystalline solids. *Phys. Rev. B* **47**, 1651–1654 (1993).
54. Heeger, A. J., Kivelson, S., Schrieffer, J. R. & Su, W. P. Solitons in conducting polymers. *Rev. Mod. Phys.* **60**, 781–850 (1988).
55. Kohn, W. Analytic properties of Bloch waves and Wannier functions. *Phys. Rev.* **115**, 809–821 (1959).
56. Schindler, F., Bradlyn, B., Fischer, M. H. & Neupert, T. Pairing obstructions in topological superconductors. *Phys. Rev. Lett.* **124**, 247001 (2020).
57. Soluyanov, A. A. & Vanderbilt, D. Wannier representation of Z_2 topological insulators. *Phys. Rev. B* **83**, 035108 (2011).
58. Bradlyn, B., Wang, Z., Cano, J. & Bernevig, B. A. Disconnected elementary band representations, fragile topology, and Wilson loops as topological indices: an example on the triangular lattice. *Phys. Rev. B* **99**, 045140 (2019).
59. Wieder, B. J. & Bernevig, B. A. The axion insulator as a pump of fragile topology. Preprint at *arXiv* https://arxiv.org/abs/1810.02373 (2018).
60. Su, W. P., Schrieffer, J. R. & Heeger, A. J. Solitons in polyacetylene. *Phys. Rev. Lett.* **42**, 1698–1701 (1979).
61. Su, W. P., Schrieffer, J. R. & Heeger, A. J. Soliton excitations in polyacetylene. *Phys. Rev. B* **22**, 2099–2111 (1980).
62. Rice, M. J. & Mele, E. J. Elementary excitations of a linearly conjugated diatomic polymer. *Phys. Rev. Lett.* **49**, 1455–1459 (1982).
63. Berry, M. V. Quantal phase factors accompanying adiabatic changes. *Proc. R. Soc. Lond. A* **392**, 45–57 (1984).
64. Zak, J. Berry's phase for energy bands in solids. *Phys. Rev. Lett.* **62**, 2747–2750 (1989).
65. Benalcazar, W. A., Bernevig, B. A. & Hughes, T. L. Quantized electric multipole insulators. *Science* **357**, 61–66 (2017).
66. Benalcazar, W. A., Bernevig, B. A. & Hughes, T. L. Electric multipole moments, topological multipole moment pumping, and chiral hinge states in crystalline insulators. *Phys. Rev. B* **96**, 245115 (2017).
67. Schindler, F. et al. Higher-order topological insulators. *Sci. Adv.* https://doi.org/10.1126/sciadv.aat0346 (2018).
68. Wieder, B. J. et al. Strong and fragile topological Dirac semimetals with higher-order fermi arcs. *Nat. Commun.* **11**, 627 (2020).
69. Wang, Z., Wieder, B. J., Li, J., Yan, B. & Bernevig, B. A. Higher-order topology, monopole nodal lines, and the origin of large Fermi arcs in transition metal dichalcogenides XTe_2 (X = Mo, W). *Phys. Rev. Lett.* **123**, 186401 (2019).
70. Benalcazar, W. A., Li, T. & Hughes, T. L. Quantization of fractional corner charge in C_n-symmetric higher-order topological crystalline insulators. *Phys. Rev. B* **99**, 245151 (2019).
71. Fidkowski, L., Jackson, T. S. & Klich, I. Model characterization of gapless edge modes of topological insulators using intermediate Brillouin-zone functions. *Phys. Rev. Lett.* **107**, 036601 (2011).
72. Yu, R., Qi, X. L., Bernevig, A., Fang, Z. & Dai, X. Equivalent expression of Z_2 topological invariant for band insulators using the non-abelian Berry connection. *Phys. Rev. B* **84**, 075119 (2011).
73. Soluyanov, A. A. & Vanderbilt, D. Computing topological invariants without inversion symmetry. *Phys. Rev. B* **83**, 235401 (2011).
74. Alexandradinata, A., Dai, X. & Bernevig, B. A. Wilson-loop characterization of inversion-symmetric topological insulators. *Phys. Rev. B* **89**, 155114 (2014).
75. Fu, L. & Kane, C. L. Time reversal polarization and a Z_2 adiabatic spin pump. *Phys. Rev. B* **74**, 195312 (2006).
76. Alexandradinata, A., Wang, Z. & Bernevig, B. A. Topological insulators from group cohomology. *Phys. Rev. X* **6**, 021008 (2016).
77. Wang, Z., Alexandradinata, A., Cava, R. J. & Bernevig, B. A. Hourglass fermions. *Nature* **532**, 189–194 (2016).
78. Wieder, B. J. et al. Wallpaper fermions and the nonsymmorphic Dirac insulator. *Science* **361**, 246–251 (2018).
79. He, L., Addison, Z., Mele, E. J. & Zhen, B. Quadrupole topological photonic crystals. *Nat. Commun.* **11**, 3119 (2020).
80. Shtyk, A. & Chamon, C. Topological electronic properties of silicon. *Phys. Rev. B* **102**, 195125 (2020).
81. Hirayama, M., Matsuishi, S., Hosono, H. & Murakami, S. Electrides as a new platform of topological materials. *Phys. Rev. X* **8**, 031067 (2018).
82. Nie, S., Bernevig, B. A. & Wang, Z. Sixfold excitations in electrides. *Phys. Rev. Res.* **3**, L012028 (2021).
83. Zhang, X. et al. Topological nodal line electrides: realization of an ideal nodal line state nearly immune from spin–orbit coupling. *J. Phys. Chem. C.* **123**, 25871–25876 (2019).
84. Nie, S. et al. Application of topological quantum chemistry in electrides. *Phys. Rev. B* **103**, 205133 (2021).
85. Cano, J. et al. Topology of disconnected elementary band representations. *Phys. Rev. Lett.* **120**, 266401 (2018).
86. Vergniory, M. G. et al. Graph theory data for topological quantum chemistry. *Phys. Rev. E* **96**, 023310 (2017).
87. Cano, J. et al. Building blocks of topological quantum chemistry: elementary band representations. *Phys. Rev. B* **97**, 035139 (2018).
88. Po, H. C., Watanabe, H. & Vishwanath, A. Fragile topology and Wannier obstructions. *Phys. Rev. Lett.* **121**, 126402 (2018).
89. Bouhon, A., Black-Schaffer, A. M. & Slager, R.-J. Wilson loop approach to fragile topology of split elementary band representations and topological crystalline insulators with time-reversal symmetry. *Phys. Rev. B* **100**, 195135 (2019).
90. Song, Z.-D., Elcoro, L., Xu, Y.-F., Regnault, N. & Bernevig, B. A. Fragile phases as affine monoids: classification and material examples. *Phys. Rev. X* **10**, 031001 (2020).
91. Hwang, Y., Ahn, J. & Yang, B.-J. Fragile topology protected by inversion symmetry: diagnosis, bulk-boundary correspondence, and Wilson loop. *Phys. Rev. B* **100**, 205126 (2019).
92. Liu, S., Vishwanath, A. & Khalaf, E. Shift insulators: rotation-protected two-dimensional topological crystalline insulators. *Phys. Rev. X* **9**, 031003 (2019).
93. Ahn, J., Park, S. & Yang, B.-J. Failure of Nielsen-Ninomiya theorem and fragile topology in two-dimensional systems with space-time inversion symmetry: Application to twisted bilayer graphene at magic angle. *Phys. Rev. X* **9**, 021013 (2019).
94. Peri, V. et al. Experimental characterization of fragile topology in an acoustic metamaterial. *Science* **367**, 797–800 (2020).
95. Song, Z.-D., Elcoro, L. & Bernevig, B. A. Twisted bulk-boundary correspondence of fragile topology. *Science* **367**, 794–797 (2020).
96. Song, Z. et al. All magic angles in twisted bilayer graphene are topological. *Phys. Rev. Lett.* **123**, 036401 (2019).
97. Zou, L., Po, H. C., Vishwanath, A. & Senthil, T. Band structure of twisted bilayer graphene: emergent symmetries, commensurate approximants, and Wannier obstructions. *Phys. Rev. B* **98**, 085435 (2018).
98. Po, H. C., Zou, L., Senthil, T. & Vishwanath, A. Faithful tight-binding models and fragile topology of magic-angle bilayer graphene. *Phys. Rev. B* **99**, 195455 (2019).
99. Taherinejad, M., Garrity, K. F. & Vanderbilt, D. Wannier center sheets in topological insulators. *Phys. Rev. B* **89**, 115102 (2014).
100. Gresch, D. et al. Z2Pack: numerical implementation of hybrid Wannier centers for identifying topological materials. *Phys. Rev. B* **95**, 075146 (2017).
101. Varnava, N., Souza, I. & Vanderbilt, D. Axion coupling in the hybrid Wannier representation. *Phys. Rev. B* **101**, 155130 (2020).
102. Zak, J. Magnetic translation group. *Phys. Rev.* **134**, A1602–A1606 (1964).
103. Niu, Q. Towards a quantum pump of electric charges. *Phys. Rev. Lett.* **64**, 1812–1815 (1990).
104. Qi, X.-L., Hughes, T. L. & Zhang, S.-C. Topological field theory of time-reversal invariant insulators. *Phys. Rev. B* **78**, 195424 (2008).
105. Moore, J. E. & Balents, L. Topological invariants of time-reversal-invariant band structures. *Phys. Rev. B* **75**, 121306 (2007).
106. Coh, S. & Vanderbilt, D. Electric polarization in a Chern insulator. *Phys. Rev. Lett.* **102**, 107603 (2009).
107. Mong, R. S. K., Essin, A. M. & Moore, J. E. Antiferromagnetic topological insulators. *Phys. Rev. B* **81**, 245209 (2010).
108. Shiozaki, K., Sato, M. & Gomi, K. Topology of nonsymmorphic crystalline insulators and superconductors. *Phys. Rev. B* **93**, 195413 (2016).
109. Franca, S., van den Brink, J. & Fulga, I. C. An anomalous higher-order topological insulator. *Phys. Rev. B* **98**, 201114 (2018).
110. Pythtb: Python tight binding open-source package. http://physics.rutgers.edu/pythtb/ (2016).
111. Qian, Y. et al. Weyl semimetals with S_4 symmetry. *Phys. Rev. B* **101**, 155143 (2020).
112. Gao, J. et al. High-throughput screening for Weyl semimetals with S_4 symmetry. *Sci. Bull.* https://www.sciencedirect.com/science/article/pii/S2095927320307738 (2020).
113. Qi, X.-L., Wu, Y.-S. & Zhang, S.-C. Topological quantization of the spin Hall effect in two-dimensional paramagnetic semiconductors. *Phys. Rev. B* **74**, 085308 (2006).

114. Fang, C., Gilbert, M. J. & Bernevig, B. A. Bulk topological invariants in noninteracting point group symmetric insulators. *Phys. Rev. B* **86**, 115112 (2012).
115. Kruthoff, J., de Boer, J., van Wezel, J., Kane, C. L. & Slager, R.-J. Topological classification of crystalline insulators through band structure combinatorics. *Phys. Rev. X* **7**, 041069 (2017).
116. Schindler, F. et al. Higher-order topology in bismuth. *Nat. Phys.* **14**, 918–924 (2018).
117. Po, H. C., Vishwanath, A. & Watanabe, H. Symmetry-based indicators of band topology in the 230 space groups. *Nat. Commun.* **8**, 50 (2017).
118. Song, Z., Fang, Z. & Fang, C. (d–2)-dimensional edge states of rotation symmetry protected topological states. *Phys. Rev. Lett.* **119**, 246402 (2017).
119. Song, Z., Zhang, T., Fang, Z. & Fang, C. Quantitative mappings between symmetry and topology in solids. *Nat. Commun.* **9**, 3530 (2018).
120. Khalaf, E., Po, H. C., Vishwanath, A. & Watanabe, H. Symmetry indicators and anomalous surface states of topological crystalline insulators. *Phys. Rev. X* **8**, 031070 (2018).
121. Song, Z., Zhang, T. & Fang, C. Diagnosis for nonmagnetic topological semimetals in the absence of spin-orbital coupling. *Phys. Rev. X* **8**, 031069 (2018).
122. Zhang, T. et al. Catalogue of topological electronic materials. *Nature* **566**, 475–479 (2019).
123. Tang, F., Po, H. C., Vishwanath, A. & Wan, X. Comprehensive search for topological materials using symmetry indicators. *Nature* **566**, 486–489 (2019).
124. Tang, F., Po, H. C., Vishwanath, A. & Wan, X. Efficient topological materials discovery using symmetry indicators. *Nat. Phys.* **15**, 470–476 (2019).
125. Haldane, F. D. M. Model for a quantum Hall effect without Landau levels: condensed-matter realization of the "parity anomaly". *Phys. Rev. Lett.* **61**, 2015–2018 (1988).
126. Castro Neto, A. H., Guinea, F., Peres, N. M. R., Novoselov, K. S. & Geim, A. K. The electronic properties of graphene. *Rev. Mod. Phys.* **81**, 109–162 (2009).
127. König, M. et al. Quantum spin Hall insulator state in HgTe quantum wells. *Science* **318**, 766–770 (2007).
128. Murakami, S. Quantum spin Hall effect and enhanced magnetic response by spin–orbit coupling. *Phys. Rev. Lett.* **97**, 236805 (2006).
129. Li, H. & Sun, K. Pfaffian formalism for higher-order topological insulators. *Phys. Rev. Lett.* **124**, 036401 (2020).
130. Marrazzo, A., Gibertini, M., Campi, D., Mounet, N. & Marzari, N. Prediction of a large-gap and switchable Kane-Mele quantum spin Hall insulator. *Phys. Rev. Lett.* **120**, 117701 (2018).
131. Wada, M., Murakami, S., Freimuth, F. & Bihlmayer, G. Localized edge states in two-dimensional topological insulators: ultrathin Bi films. *Phys. Rev. B* **83**, 121310 (2011).
132. Drozdov, I. K. et al. One-dimensional topological edge states of bismuth bilayers. *Nat. Phys.* **10**, 664–669 (2014).
133. Reis, F. et al. Bismuthene on a SiC substrate: a candidate for a high-temperature quantum spin Hall material. *Science* **357**, 287–290 (2017).
134. Varsano, D., Palummo, M., Molinari, E. & Rontani, M. A monolayer transition-metal dichalcogenide as a topological excitonic insulator. *Nat. Nanotechnol.* **15**, 367–372 (2020).
135. Qian, X., Liu, J., Fu, L. & Li, J. Quantum spin Hall effect in two-dimensional transition metal dichalcogenides. *Science* **346**, 1344–1347 (2014).
136. Wu, S. et al. Observation of the quantum spin Hall effect up to 100 kelvin in a monolayer crystal. *Science* **359**, 76–79 (2018).
137. Tang, S. et al. Quantum spin Hall state in monolayer 1T′-WTe_2. *Nat. Phys.* **13**, 683–687 (2017).
138. Guo, Z. et al. Quantum spin Hall effect in $Ta_2M_3Te_5$ (M = Pd, Ni). *Phys. Rev. B* **103**, 115145 (2021).
139. Wang, X. et al. Observation of quantum spin Hall states in $Ta_2Pd_3Te_5$. Preprint at *arXiv* https://arxiv.org/abs/2012.07293 (2020).
140. Marrazzo, A., Marzari, N. & Gibertini, M. Emergent dual topology in the three-dimensional Kane-Mele Pt_2HgSe_3. *Phys. Rev. Res.* **2**, 012063 (2020).
141. Facio, J. I. et al. Dual topology in Jacutingaite Pt_2HgSe_3. *Phys. Rev. Mater.* **3**, 074202 (2019).
142. Cucchi, I. et al. Bulk and surface electronic structure of the dual-topology semimetal Pt_2HgSe_3. *Phys. Rev. Lett.* **124**, 106402 (2020).
143. Fu, L., Kane, C. L. & Mele, E. J. Topological insulators in three dimensions. *Phys. Rev. Lett.* **98**, 106803 (2007).
144. Roy, R. Topological phases and the quantum spin Hall effect in three dimensions. *Phys. Rev. B* **79**, 195322 (2009).
145. Hsieh, D. et al. A topological Dirac insulator in a quantum spin Hall phase. *Nature* **452**, 970–974 (2008).
146. Hsieh, D. et al. Observation of unconventional quantum spin textures in topological insulators. *Science* **323**, 919–922 (2009).
147. Xia, Y. et al. Observation of a large-gap topological-insulator class with a single Dirac cone on the surface. *Nat. Phys.* **5**, 398–402 (2009).
148. Hsieh, D. et al. Observation of time-reversal-protected single-Dirac-cone topological-insulator states in Bi_2Te_3 and Sb_2Te_3. *Phys. Rev. Lett.* **103**, 146401 (2009).
149. Zhang, H. et al. Topological insulators in Bi_2Se_3, Bi_2Te_3 and Sb_2Te_3 with a single Dirac cone on the surface. *Nat. Phys.* **5**, 438–442 (2009).
150. Hsieh, D. et al. A tunable topological insulator in the spin helical Dirac transport regime. *Nature* **460**, 1101–1105 (2009).
151. Eschbach, M. et al. Realization of a vertical topological p–n junction in epitaxial Sb_2Te_3/Bi_2Te_3 heterostructures. *Nat. Commun.* **6**, 8816 (2015).
152. Zhao, L. et al. Emergent surface superconductivity in the topological insulator Sb_2Te_3. *Nat. Commun.* **6**, 8279 (2015).
153. Yang, H. et al. Visualizing electronic structures of quantum materials by angle-resolved photoemission spectroscopy. *Nat. Rev. Mater.* **3**, 341–353 (2018).
154. Lv, B., Qian, T. & Ding, H. Angle-resolved photoemission spectroscopy and its application to topological materials. *Nat. Rev. Phys.* **1**, 609–626 (2019).
155. Roushan, P. et al. Topological surface states protected from backscattering by chiral spin texture. *Nature* **460**, 1106–1109 (2009).
156. Ringel, Z., Kraus, Y. E. & Stern, A. Strong side of weak topological insulators. *Phys. Rev. B* **86**, 045102 (2012).
157. Liu, C.-X., Qi, X.-L. & Zhang, S.-C. Half quantum spin Hall effect on the surface of weak topological insulators. *Phys. E* **44**, 906–911 (2012).
158. Liu, C.-C., Zhou, J.-J., Yao, Y. & Zhang, F. Weak topological insulators and composite Weyl semimetals: β–Bi_4X_4 (X = Br, I). *Phys. Rev. Lett.* **116**, 066801 (2016).
159. Noguchi, R. et al. A weak topological insulator state in quasi-one-dimensional bismuth iodide. *Nature* **566**, 518–522 (2019).
160. Weng, H., Dai, X. & Fang, Z. Transition-metal pentatelluride $ZrTe_5$ and $HfTe_5$: a paradigm for large-gap quantum spin Hall insulators. *Phys. Rev. X* **4**, 011002 (2014).
161. Zhang, P. et al. Observation and control of the weak topological insulator state in $ZrTe_5$. *Nat. Commun.* **12**, 406 (2021).
162. Rasche, B. et al. Crystal growth and real structure effects of the first weak 3D stacked topological insulator $Bi_{14}Rh_3I_9$. *Chem. Mater.* **25**, 2359–2364 (2013).
163. Rasche, B. et al. Stacked topological insulator built from bismuth-based graphene sheet analogues. *Nat. Mater.* **12**, 422–425 (2013).
164. Pauly, C. et al. Subnanometre-wide electron channels protected by topology. *Nat. Phys.* **11**, 338–343 (2015).
165. Lee, K. et al. Discovery of a weak topological insulating state and Van Hove singularity in triclinic $RhBi_2$. *Nat. Commun.* **12**, 1855 (2021).
166. Ruck, M. Kristallstruktur und Zwillingsbildung der intermetallischen phase β-Bi_2Rh. *Acta Crystallogr. B* **52**, 605–609 (1996).
167. Hsieh, T. H. et al. Topological crystalline insulators in the SnTe material class. *Nat. Commun.* **3**, 982 (2012).
168. Tanaka, Y. et al. Experimental realization of a topological crystalline insulator in SnTe. *Nat. Phys.* **8**, 800–803 (2012).
169. Fang, C. & Fu, L. New classes of topological crystalline insulators having surface rotation anomaly. *Sci. Adv.* **5**, eaat2374 (2019).
170. Fu, L. Topological crystalline insulators. *Phys. Rev. Lett.* **106**, 106802 (2011).
171. Teo, J. C. Y., Fu, L. & Kane, C. L. Surface states and topological invariants in three-dimensional topological insulators: application to $Bi_{1-x}Sb_x$. *Phys. Rev. B* **78**, 045426 (2008).
172. Dong, X.-Y. & Liu, C.-X. Classification of topological crystalline insulators based on representation theory. *Phys. Rev. B* **93**, 045429 (2016).
173. Slager, R.-J., Mesaros, A., Juričć, V. & Zaanen, J. The space group classification of topological band-insulators. *Nat. Phys.* **9**, 98–102 (2013).
174. Shiozaki, K., Sato, M. & Gomi, K. Topological crystalline materials: general formulation, module structure, and wallpaper groups. *Phys. Rev. B* **95**, 235425 (2017).
175. Fang, C. & Fu, L. New classes of three-dimensional topological crystalline insulators: nonsymmorphic and magnetic. *Phys. Rev. B* **91**, 161105 (2015).
176. Ma, J. et al. Experimental evidence of hourglass fermion in the candidate nonsymmorphic topological insulator KHgSb. *Sci. Adv.* https://doi.org/10.1126/sciadv.1602415 (2017).
177. Liang, S. et al. A gap-protected zero-Hall effect state in the quantum limit of the non-symmorphic metal KHgSb. *Nat. Mater.* **18**, 443–447 (2019).
178. Robredo, I. N., Vergniory, M. G. & Bradlyn, B. Higher-order and crystalline topology in a phenomenological tight-binding model of lead telluride. *Phys. Rev. Mater.* **3**, 041202 (2019).
179. Fang, Y. & Cano, J. Higher-order topological insulators in antiperovskites. *Phys. Rev. B* **101**, 245110 (2020).
180. Zhou, X. et al. Glide-mirror protected first- and second-order topological crystalline insulator. Preprint at *arXiv* https://arxiv.org/abs/2005.06071 (2020).
181. Liu, Y. & Allen, R. E. Electronic structure of the semimetals Bi and Sb. *Phys. Rev. B* **52**, 1566–1577 (1995).
182. Wallace, P. R. The band theory of graphite. *Phys. Rev.* **71**, 622–634 (1947).
183. Semenoff, G. W. Condensed-matter simulation of a three-dimensional anomaly. *Phys. Rev. Lett.* **53**, 2449–2452 (1984).
184. DiVincenzo, D. P. & Mele, E. J. Self-consistent effective-mass theory for intralayer screening in graphite intercalation compounds. *Phys. Rev. B* **29**, 1685–1694 (1984).
185. Ruffieux, P. et al. On-surface synthesis of graphene nanoribbons with zigzag edge topology. *Nature* **531**, 489–492 (2016).
186. Fujita, M., Wakabayashi, K., Nakada, K. & Kusakabe, K. Peculiar localized state at zigzag graphite edge. *J. Phys. Soc. Jpn.* **65**, 1920–1923 (1996).
187. Nakada, K., Fujita, M., Dresselhaus, G. & Dresselhaus, M. S. Edge state in graphene ribbons: nanometer size effect and edge shape dependence. *Phys. Rev. B* **54**, 17954–17961 (1996).
188. Zhang, F. Spontaneous chiral symmetry breaking in bilayer graphene. *Synth. Met.* **210**, 9–18 (2015).
189. Zhang, F., Kane, C. L. & Mele, E. J. Surface states of topological insulators. *Phys. Rev. B* **86**, 081303 (2012).
190. Alvarez-Gaumé, L. & Witten, E. Gravitational anomalies. *Nucl. Phys. B* **234**, 269–330 (1984).
191. Redlich, A. N. Gauge noninvariance and parity nonconservation of three-dimensional fermions. *Phys. Rev. Lett.* **52**, 18–21 (1984).
192. Jackiw, R. Fractional charge and zero modes for planar systems in a magnetic field. *Phys. Rev. D.* **29**, 2375–2377 (1984).
193. Mañes, J. L. Existence of bulk chiral fermions and crystal symmetry. *Phys. Rev. B* **85**, 155118 (2012).
194. Young, S. M. et al. Dirac semimetal in three dimensions. *Phys. Rev. Lett.* **108**, 140405 (2012).
195. Wieder, B. J. & Kane, C. L. Spin-orbit semimetals in the layer groups. *Phys. Rev. B* **94**, 155108 (2016).
196. Watanabe, H., Po, H. C., Vishwanath, A. & Zaletel, M. Filling constraints for spin-orbit coupled insulators in symmorphic and nonsymmorphic crystals. *Proc. Natl Acad. Sci. USA* **112**, 14551–14556 (2015).
197. Watanabe, H., Po, H. C., Zaletel, M. P. & Vishwanath, A. Filling-enforced gaplessness in band structures of the 230 space groups. *Phys. Rev. Lett.* **117**, 096404 (2016).
198. Steinberg, J. A. et al. Bulk Dirac points in distorted spinels. *Phys. Rev. Lett.* **112**, 036403 (2014).
199. Wang, Z., Weng, H., Wu, Q., Dai, X. & Fang, Z. Three-dimensional Dirac semimetal and quantum transport in Cd_3As_2. *Phys. Rev. B* **88**, 125427 (2013).
200. Wang, Z. et al. Dirac semimetal and topological phase transitions in A_3Bi (A = Na, K, Rb). *Phys. Rev. B* **85**, 195320 (2012).
201. Borisenko, S. et al. Experimental realization of a three-dimensional Dirac semimetal. *Phys. Rev. Lett.* **113**, 027603 (2014).
202. Ali, M. N. et al. The crystal and electronic structures of Cd_3As_2, the three-dimensional electronic analogue of graphene. *Inorg. Chem.* **53**, 4062–4067 (2014).
203. Liu, Z. K. et al. A stable three-dimensional topological Dirac semimetal Cd_3As_2. *Nat. Mater.* **13**, 677–681 (2014).
204. Liu, Z. K. et al. Discovery of a three-dimensional topological Dirac semimetal, Na_3Bi. *Science* **343**, 864–867 (2014).
205. Chang, T.-R. et al. Type-II symmetry-protected topological Dirac semimetals. *Phys. Rev. Lett.* **119**, 026404 (2017).
206. Guo, P.-J., Yang, H.-C., Liu, K. & Lu, Z.-Y. Type-II Dirac semimetals in the YPd_2Sn class. *Phys. Rev. B* **95**, 155112 (2017).
207. Yan, M. et al. Lorentz-violating type-II Dirac fermions in transition metal dichalcogenide $PtTe_2$. *Nat. Commun.* **8**, 257 (2017).

208. Xu, S.-Y. et al. Observation of Fermi arc surface states in a topological metal. *Science* https://doi.org/10.1126/science.1256742 (2014).
209. Yi, H. et al. Evidence of topological surface state in three-dimensional Dirac semimetal Cd_3As_2. *Sci. Rep.* **4**, 6106 (2014).
210. Potter, A. C., Kimchi, I. & Vishwanath, A. Quantum oscillations from surface Fermi arcs in Weyl and Dirac semimetals. *Nat. Commun.* **5**, 5161 (2014).
211. Chiu, C.-K. & Schnyder, A. P. Classification of crystalline topological semimetals with an application to Na_3Bi. *J. Phys. Conf. Ser.* **603**, 012002 (2015).
212. Yang, B.-J. & Nagaosa, N. Classification of stable three-dimensional Dirac semimetals with nontrivial topology. *Nat. Commun.* **5**, 4898 (2014).
213. Wu, Y. et al. Dirac node arcs in $PtSn_4$. *Nat. Phys.* **12**, 667–671 (2016).
214. Moll, P. J. W. et al. Transport evidence for Fermi-arc-mediated chirality transfer in the Dirac semimetal Cd_3As_2. *Nature* **535**, 266–270 (2016).
215. Gyenis, A. et al. Imaging electronic states on topological semimetals using scanning tunneling microscopy. *N. J. Phys.* **18**, 105003 (2016).
216. Jeon, S. et al. Landau quantization and quasiparticle interference in the three-dimensional Dirac semimetal Cd_3As_2. *Nat. Mater.* **13**, 851–856 (2014).
217. Kargarian, M., Randeria, M. & Lu, Y.-M. Are the surface Fermi arcs in Dirac semimetals topologically protected? *Proc. Natl Acad. Sci. USA* **113**, 8648–8652 (2016).
218. Kargarian, M., Lu, Y.-M. & Randeria, M. Deformation and stability of surface states in Dirac semimetals. *Phys. Rev. B* **97**, 165129 (2018).
219. Le, C. et al. Dirac semimetal in β-CuI without surface Fermi arcs. *Proc. Natl Acad. Sci. USA* **115**, 8311–8315 (2018).
220. Murakami, S. Phase transition between the quantum spin Hall and insulator phases in 3D: emergence of a topological gapless phase. *N. J. Phys.* **9**, 356–356 (2007).
221. Wan, X., Turner, A. M., Vishwanath, A. & Savrasov, S. Y. Topological semimetal and Fermi-arc surface states in the electronic structure of pyrochlore iridates. *Phys. Rev. B* **83**, 205101 (2011).
222. Burkov, A. A. & Balents, L. Weyl semimetal in a topological insulator multilayer. *Phys. Rev. Lett.* **107**, 127205 (2011).
223. Weng, H., Fang, C., Fang, Z., Bernevig, B. A. & Dai, X. Weyl semimetal phase in noncentrosymmetric transition-metal monophosphides. *Phys. Rev. X* **5**, 011029 (2015).
224. Huang, S.-M. et al. A Weyl fermion semimetal with surface Fermi arcs in the transition metal monopnictide TaAs class. *Nat. Commun.* **6**, 7373 (2015).
225. Xu, S.-Y. et al. Discovery of a Weyl fermion semimetal and topological Fermi arcs. *Science* **349**, 613–617 (2015).
226. Lv, B. Q. et al. Experimental discovery of Weyl semimetal TaAs. *Phys. Rev. X* **5**, 031013 (2015).
227. Yang, L. X. et al. Weyl semimetal phase in the non-centrosymmetric compound TaAs. *Nat. Phys.* **11**, 728–732 (2015).
228. Inoue, H. et al. Quasiparticle interference of the Fermi arcs and surface-bulk connectivity of a Weyl semimetal. *Science* **351**, 1184–1187 (2016).
229. Soluyanov, A. A. et al. Type-II Weyl semimetals. *Nature* **527**, 495–498 (2015).
230. Wang, Z. et al. MoTe2: a type-II Weyl topological metal. *Phys. Rev. Lett.* **117**, 056805 (2016).
231. Huang, S.-M. et al. New type of Weyl semimetal with quadratic double Weyl fermions. *Proc. Natl Acad. Sci. USA* **113**, 1180–1185 (2016).
232. Tsirkin, S. S., Souza, I. & Vanderbilt, D. Composite Weyl nodes stabilized by screw symmetry with and without time-reversal invariance. *Phys. Rev. B* **96**, 045102 (2017).
233. Fang, C., Gilbert, M. J., Dai, X. & Bernevig, B. A. Multi-Weyl topological semimetals stabilized by point group symmetry. *Phys. Rev. Lett.* **108**, 266802 (2012).
234. Xu, G., Weng, H., Wang, Z., Dai, X. & Fang, Z. Chern semimetal and the quantized anomalous Hall effect in $HgCr_2Se_4$. *Phys. Rev. Lett.* **107**, 186806 (2011).
235. Chang, G. et al. Topological quantum properties of chiral crystals. *Nat. Mater.* **17**, 978–985 (2018).
236. Bernevig, B. A. *Weyl Semimetals* https://www.youtube.com/watch?v=j0zgWHLL1z4 (Topological Matter School DIPC, 2016).
237. Gatti, G. et al. Radial spin texture of the Weyl fermions in chiral tellurium. *Phys. Rev. Lett.* **125**, 216402 (2020).
238. Zhang, C.-L. et al. Ultraquantum magnetoresistance in the Kramers-Weyl semimetal candidate β–Ag_2Se. *Phys. Rev. B* **96**, 165148 (2017).
239. Qiu, G. et al. Quantum Hall effect of Weyl fermions in n-type semiconducting tellurene. *Nat. Nanotechnol.* **15**, 585–591 (2020).
240. Liu, Q.-B., Qian, Y., Fu, H.-H. & Wang, Z. Symmetry-enforced Weyl phonons. *npj Comput. Mater.* **6**, 95 (2020).
241. Gooth, J. et al. Experimental signatures of the mixed axial–gravitational anomaly in the Weyl semimetal NbP. *Nature* **547**, 324–327 (2017).
242. Franz, M. & Rozali, M. Mimicking black hole event horizons in atomic and solid-state systems. *Nat. Rev. Mater.* **3**, 491–501 (2018).
243. Nielsen, H. & Ninomiya, M. The Adler-Bell-Jackiw anomaly and Weyl fermions in a crystal. *Phys. Lett. B* **130**, 389–396 (1983).
244. Son, D. T. & Spivak, B. Z. Chiral anomaly and classical negative magnetoresistance of Weyl metals. *Phys. Rev. B* **88**, 104412 (2013).
245. Xiong, J. et al. Evidence for the chiral anomaly in the dirac semimetal Na_3Bi. *Science* **350**, 413–416 (2015).
246. Huang, X. et al. Observation of the chiral-anomaly-induced negative magnetoresistance in 3D Weyl semimetal TaAs. *Phys. Rev. X* **5**, 031023 (2015).
247. Liang, S. et al. Experimental tests of the chiral anomaly magnetoresistance in the Dirac-Weyl semimetals Na_3Bi and GdPtBi. *Phys. Rev. X* **8**, 031002 (2018).
248. Hirschberger, M. et al. The chiral anomaly and thermopower of Weyl fermions in the half-Heusler GdPtBi. *Nat. Mater.* **15**, 1161–1165 (2016).
249. Zhang, C.-L. et al. Signatures of the Adler-Bell-Jackiw chiral anomaly in a Weyl fermion semimetal. *Nat. Commun.* **7**, 10735 (2016).
250. Cano, J. et al. Chiral anomaly factory: Creating Weyl fermions with a magnetic field. *Phys. Rev. B* **95**, 161306 (2017).
251. Kim, Y., Wieder, B. J., Kane, C. L. & Rappe, A. M. Dirac line nodes in inversion-symmetric crystals. *Phys. Rev. Lett.* **115**, 036806 (2015).
252. Yu, R., Weng, H., Fang, Z., Dai, X. & Hu, X. Topological node-line semimetal and Dirac semimetal state in antiperovskite Cu_3PdN. *Phys. Rev. Lett.* **115**, 036807 (2015).
253. Fang, C., Chen, Y., Kee, H.-Y. & Fu, L. Topological nodal line semimetals with and without spin-orbital coupling. *Phys. Rev. B* **92**, 081201 (2015).
254. Wieder, B. J., Kim, Y., Rappe, A. M. & Kane, C. L. Double Dirac semimetals in three dimensions. *Phys. Rev. Lett.* **116**, 186402 (2016).
255. Bradlyn, B. et al. Beyond Dirac and Weyl fermions: unconventional quasiparticles in conventional crystals. *Science* **353**, aaf5037 (2016).
256. Carter, J.-M., Shankar, V. V., Zeb, M. A. & Kee, H.-Y. Semimetal and topological insulator in perovskite iridates. *Phys. Rev. B* **85**, 115105 (2012).
257. Bzdušek, T., Wu, Q., Rüegg, A., Sigrist, M. & Soluyanov, A. A. Nodal-chain metals. *Nature* **538**, 75–78 (2016).
258. Wu, Q., Soluyanov, A. A. & Bzdušek, T. Non-abelian band topology in noninteracting metals. *Science* **365**, 1273–1277 (2019).
259. Xie, L. S. et al. A new form of Ca_3P_2 with a ring of Dirac nodes. *Appl. Mater.* **3**, 083602 (2015).
260. Schoop, L. M. et al. Dirac cone protected by non-symmorphic symmetry and three-dimensional Dirac line node in ZrSiS. *Nat. Commun.* **7**, 11696 (2016).
261. Topp, A. et al. Surface floating 2D bands in layered nonsymmorphic semimetals: ZrSiS and related compounds. *Phys. Rev. X* **7**, 041073 (2017).
262. Takane, D. et al. Observation of Dirac-like energy band and ring-torus Fermi surface associated with the nodal line in topological insulator CaAgAs. *npj Quant. Mater.* **3**, 1 (2018).
263. Bian, G. et al. Topological nodal-line fermions in spin-orbit metal $PbTaSe_2$. *Nat. Commun.* **7**, 10556 (2016).
264. Lou, R. et al. Experimental observation of bulk nodal lines and electronic surface states in ZrB_2. *npj Quant. Mater.* **3**, 43 (2018).
265. Shao, Y. et al. Optical signatures of Dirac nodal lines in $NbAs_2$. *Proc. Natl Acad. Sci. USA* **116**, 1168–1173 (2019).
266. Zhu, Z. et al. Quasiparticle interference and nonsymmorphic effect on a floating band surface state of ZrSiSe. *Nat. Commun.* **9**, 4153 (2018).
267. Sharma, G. et al. Electronic structure, photovoltage, and photocatalytic hydrogen evolution with p-$CuBi_2O_4$ nanocrystals. *J. Mater. Chem. A* **4**, 2936–2942 (2016).
268. Di Sante, D. et al. Realizing double Dirac particles in the presence of electronic interactions. *Phys. Rev. B* **96**, 121106 (2017).
269. Weng, H., Fang, C., Fang, Z. & Dai, X. Topological semimetals with triply degenerate nodal points in θ-phase tantalum nitride. *Phys. Rev. B* **93**, 241202 (2016).
270. Zhu, Z., Winkler, G. W., Wu, Q., Li, J. & Soluyanov, A. A. Triple point topological metals. *Phys. Rev. X* **6**, 031003 (2016).
271. Chang, G. et al. Nexus fermions in topological symmorphic crystalline metals. *Sci. Rep.* **7**, 1688–1688 (2017).
272. Lv, B. Q. et al. Observation of three-component fermions in the topological semimetal molybdenum phosphide. *Nature* **546**, 627–631 (2017).
273. Ma, J.-Z. et al. Three-component fermions with surface Fermi arcs in tungsten carbide. *Nat. Phys.* **14**, 349–354 (2018).
274. Gao, H. et al. Dirac-weyl semimetal: coexistence of Dirac and Weyl fermions in polar hexagonal *abc* crystals. *Phys. Rev. Lett.* **121**, 106404 (2018).
275. Sun, Z. P. et al. Direct observation of sixfold exotic fermions in the pyrite-structured topological semimetal $PdSb_2$. *Phys. Rev. B* **101**, 155114 (2020).
276. Wieder, B. J. Threes company. *Nat. Phys.* **14**, 329–330 (2018).
277. Chang, G. et al. Unconventional chiral fermions and large topological Fermi arcs in RhSi. *Phys. Rev. Lett.* **119**, 206401 (2017).
278. Tang, P., Zhou, Q. & Zhang, S.-C. Multiple types of topological fermions in transition metal silicides. *Phys. Rev. Lett.* **119**, 206402 (2017).
279. Takane, D. et al. Observation of chiral fermions with a large topological charge and associated Fermi-arc surface states in CoSi. *Phys. Rev. Lett.* **122**, 076402 (2019).
280. Sanchez, D. S. et al. Topological chiral crystals with helicoid-arc quantum states. *Nature* **567**, 500–505 (2019).
281. Rao, Z. et al. Observation of unconventional chiral fermions with long Fermi arcs in CoSi. *Nature* **567**, 496–499 (2019).
282. Schröter, N. B. M. et al. Chiral topological semimetal with multifold band crossings and long Fermi arcs. *Nat. Phys.* **15**, 759–765 (2019).
283. Yuan, Q.-Q. et al. Quasiparticle interference evidence of the topological Fermi arc states in chiral fermionic semimetal CoSi. *Sci. Adv.* **5**, eaaw9485 (2019).
284. Schröter, N. B. M. et al. Observation and control of maximal Chern numbers in a chiral topological semimetal. *Science* **369**, 179–183 (2020).
285. Yao, M. et al. Observation of giant spin-split Fermi-arc with maximal Chern number in the chiral topological semimetal PtGa. *Nat. Commun.* **11**, 2033 (2020).
286. Li, H. et al. Chiral fermion reversal in chiral crystals. *Nat. Commun.* **10**, 5505 (2019).
287. Lv, B. Q. et al. Observation of multiple types of topological fermions in PdBiSe. *Phys. Rev. B* **99**, 241104 (2019).
288. Gao, J. Z. S. et al. Topological superconductivity in multifold fermion metals. Preprint at *arXiv* https://arxiv.org/abs/2012.11287 (2020).
289. Emmanouilidou, E. et al. Fermiology and type-I superconductivity in the chiral superconductor $NbGe_2$ with Kramers-Weyl fermions. *Phys. Rev. B* **102**, 235144 (2020).
290. de Juan, F., Grushin, A. G., Morimoto, T. & Moore, J. E. Quantized circular photogalvanic effect in Weyl semimetals. *Nat. Commun.* **8**, 15995 (2017).
291. Flicker, F. et al. Chiral optical response of multifold fermions. *Phys. Rev. B* **98**, 155145 (2018).
292. Chang, G. et al. Unconventional photocurrents from surface Fermi arcs in topological chiral semimetals. *Phys. Rev. Lett.* **124**, 166404 (2020).
293. Rees, D. et al. Helicity-dependent photocurrents in the chiral Weyl semimetal RhSi. *Sci. Adv.* **6**, eaba0509 (2020).
294. Ni, Z. et al. Giant topological longitudinal circular photo-galvanic effect in the chiral multifold semimetal CoSi. *Nat. Commun.* **12**, 154 (2021).
295. Rebar, D. J. et al. Fermi surface, possible unconventional fermions, and unusually robust resistive critical fields in the chiral-structured superconductor AuBe. *Phys. Rev. B* **99**, 094517 (2019).
296. Zak, J. Band representations and symmetry types of bands in solids. *Phys. Rev. B* **23**, 2824–2835 (1981).
297. Zak, J. Band representations of space groups. *Phys. Rev. B* **26**, 3010–3023 (1982).
298. Smith, H. J. S. & Sylvester, J. J. XV. On systems of linear indeterminate equations and congruences. *Phil. Trans. R. Soc. Lond.* **151**, 293–326 (1861).
299. Elcoro, L. et al. Magnetic topological quantum chemistry. *Nat. Commun.* **12**, 5965 (2021).
300. Xu, Y. et al. High-throughput calculations of magnetic topological materials. *Nature* **586**, 702–707 (2020).
301. Po, H. C. Symmetry indicators of band topology. *J. Phys. Condens. Matter* **32**, 263001 (2020).

302. Cano, J. & Bradlyn, B. Band representations and topological quantum chemistry. *Annu. Rev. Condens. Matter Phys.* **12**, 225–246 (2021).
303. Teo, J. C. Y. & Kane, C. L. Topological defects and gapless modes in insulators and superconductors. *Phys. Rev. B* **82**, 115120 (2010).
304. Ran, Y., Zhang, Y. & Vishwanath, A. One-dimensional topologically protected modes in topological insulators with lattice dislocations. *Nat. Phys.* **5**, 298–303 (2009).
305. Zhang, F., Kane, C. L. & Mele, E. J. Surface state magnetization and chiral edge states on topological insulators. *Phys. Rev. Lett.* **110**, 046404 (2013).
306. Seradjeh, B., Weeks, C. & Franz, M. Fractionalization in a square-lattice model with time-reversal symmetry. *Phys. Rev. B* **77**, 033104 (2008).
307. Benalcazar, W. A., Teo, J. C. Y. & Hughes, T. L. Classification of two-dimensional topological crystalline superconductors and Majorana bound states at disclinations. *Phys. Rev. B* **89**, 224503 (2014).
308. Khalaf, E. Higher-order topological insulators and superconductors protected by inversion symmetry. *Phys. Rev. B* **97**, 205136 (2018).
309. Langbehn, J., Peng, Y., Trifunovic, L., von Oppen, F. & Brouwer, P. W. Reflection-symmetric second-order topological insulators and superconductors. *Phys. Rev. Lett.* **119**, 246401 (2017).
310. Trifunovic, L. & Brouwer, P. W. Higher-order bulk-boundary correspondence for topological crystalline phases. *Phys. Rev. X* **9**, 011012 (2019).
311. Murani, A. et al. Ballistic edge states in bismuth nanowires revealed by SQUID interferometry. *Nat. Commun.* **8**, 15941 (2017).
312. Nayak, A. K. et al. Resolving the topological classification of bismuth with topological defects. *Sci. Adv.* **5**, eaax6996 (2019).
313. Queiroz, R., Fulga, I. C., Avraham, N., Beidenkopf, H. & Cano, J. Partial lattice defects in higher-order topological insulators. *Phys. Rev. Lett.* **123**, 266802 (2019).
314. Wang, W. et al. Evidence for an edge supercurrent in the Weyl superconductor $MoTe_2$. *Science* **368**, 534–537 (2020).
315. Choi, Y.-B. et al. Evidence of higher-order topology in multilayer WTe_2 from Josephson coupling through anisotropic hinge states. *Nat. Mater.* https://doi.org/10.1038/s41563-020-0721-9 (2020).
316. Kononov, A. et al. One-dimensional edge transport in few-layer WTe_2. *Nano Lett.* **20**, 4228–4233 (2020).
317. Huang, C. et al. Edge superconductivity in multilayer WTe_2 Josephson junction. *Natl Sci. Rev.* **7**, 1468–1475 (2020).
318. Huang, F.-T. et al. Polar and phase domain walls with conducting interfacial states in a Weyl semimetal $MoTe_2$. *Nat. Commun.* **10**, 4211 (2019).
319. Noguchi, R. et al. Evidence for a higher-order topological insulator in a three-dimensional material built from van der Waals stacking of bismuth-halide chains. *Nat. Mater.* **20**, 473–479 (2021).
320. Mao, P. et al. Observation of the topologically originated edge states in large-gap quasi-one-dimensional a-Bi_4Br_4. Preprint at *arXiv* https://arxiv.org/abs/2007.00223 (2020).
321. Mao, P. et al. Ultralong carrier lifetime of topological edge states in a-Bi_4Br_4. Preprint at *arXiv* https://arxiv.org/abs/2007.00264 (2020).
322. Hsu, C.-H. et al. Purely rotational symmetry-protected topological crystalline insulator α-Bi_4Br_4. *2D Mater.* **6**, 031004 (2019).
323. Yoon, C., Liu, C.-C., Min, H. & Zhang, F. Quasi-one-dimensional higher-order topological insulators. Preprint at *arXiv* https://arxiv.org/abs/2005.14710 (2020).
324. Hughes, T. L., Prodan, E. & Bernevig, B. A. Inversion-symmetric topological insulators. *Phys. Rev. B* **83**, 245132 (2011).
325. Turner, A. M., Zhang, Y., Mong, R. S. K. & Vishwanath, A. Quantized response and topology of magnetic insulators with inversion symmetry. *Phys. Rev. B* **85**, 165120 (2012).
326. Chen, X., Fidkowski, L. & Vishwanath, A. Symmetry enforced non-abelian topological order at the surface of a topological insulator. *Phys. Rev. B* **89**, 165132 (2014).
327. Turner, A. M., Zhang, Y. & Vishwanath, A. Entanglement and inversion symmetry in topological insulators. *Phys. Rev. B* **82**, 241102 (2010).
328. Coh, S. & Vanderbilt, D. Canonical magnetic insulators with isotropic magnetoelectric coupling. *Phys. Rev. B* **88**, 121106 (2013).
329. Essin, A. M., Moore, J. E. & Vanderbilt, D. Magnetoelectric polarizability and axion electrodynamics in crystalline insulators. *Phys. Rev. Lett.* **102**, 146805 (2009).
330. Wilczek, F. Two applications of axion electrodynamics. *Phys. Rev. Lett.* **58**, 1799–1802 (1987).
331. Witten, E. Dyons of charge eθ/2π. *Phys. Lett. B* **86**, 283–287 (1979).
332. Wu, L. et al. Quantized Faraday and Kerr rotation and axion electrodynamics of a 3D topological insulator. *Science* **354**, 1124–1127 (2016).
333. Watanabe, H., Po, H. C. & Vishwanath, A. Structure and topology of band structures in the 1651 magnetic space groups. *Sci. Adv.* **4**, eaat8685 (2018).
334. Ahn, J. & Yang, B.-J. Symmetry representation approach to topological invariants in $C_{2z}T$-symmetric systems. *Phys. Rev. B* **99**, 235125 (2019).
335. Yue, C. et al. Symmetry-enforced chiral hinge states and surface quantum anomalous Hall effect in the magnetic axion insulator $Bi_{2-x}Sm_xSe_3$. *Nat. Phys.* **15**, 577–581 (2019).
336. Zhang, D. et al. Topological axion states in the magnetic insulator $MnBi_2Te_4$ with the quantized magnetoelectric effect. *Phys. Rev. Lett.* **122**, 206401 (2019).
337. Li, J. et al. Intrinsic magnetic topological insulators in van der Waals layered $MnBi_2Te_4$-family materials. *Sci. Adv.* **5**, eaaw5685 (2019).
338. Mogi, M. et al. A magnetic heterostructure of topological insulators as a candidate for an axion insulator. *Nat. Mater.* **16**, 516–521 (2017).
339. Xiao, D. et al. Realization of the axion insulator state in quantum anomalous Hall sandwich heterostructures. *Phys. Rev. Lett.* **120**, 056801 (2018).
340. Otrokov, M. M. et al. Prediction and observation of an antiferromagnetic topological insulator. *Nature* **576**, 416–422 (2019).
341. Gong, Y. et al. Experimental realization of an intrinsic magnetic topological insulator. *Chin. Phys. Lett.* **36**, 076801 (2019).
342. Lin, M. & Hughes, T. L. Topological quadrupolar semimetals. *Phys. Rev. B* **98**, 241103 (2018).
343. Li, C.-Z. et al. Reducing electronic transport dimension to topological hinge states by increasing geometry size of Dirac semimetal Josephson junctions. *Phys. Rev. Lett.* **124**, 156601 (2020).
344. Ahn, J., Kim, D., Kim, Y. & Yang, B.-J. Band topology and linking structure of nodal line semimetals with Z_2 monopole charges. *Phys. Rev. Lett.* **121**, 106403 (2018).
345. Ghorashi, S. A. A., Li, T. & Hughes, T. L. Higher-order Weyl semimetals. *Phys. Rev. Lett.* **125**, 266804 (2020).
346. Jain, A. et al. Commentary: The materials project: a materials genome approach to accelerating materials innovation. *Appl. Mater.* **1**, 011002 (2013).
347. Hohenberg, P. & Kohn, W. Inhomogeneous electron gas. *Phys. Rev.* **136**, B864–B871 (1964).
348. Kohn, W. & Sham, L. J. Self-consistent equations including exchange and correlation effects. *Phys. Rev.* **140**, A1133–A1138 (1965).
349. Kresse, G. & Joubert, D. From ultrasoft pseudopotentials to the projector augmented-wave method. *Phys. Rev. B* **59**, 1758–1775 (1999).
350. Kresse, G. & Hafner, J. *Ab initio* molecular dynamics for open-shell transition metals. *Phys. Rev. B* **48**, 13115–13118 (1993).
351. Gao, J., Wu, Q., Persson, C. & Wang, Z. Irvsp: To obtain irreducible representations of electronic states in the VASP. *Comput. Phys. Commun.* **261**, 107760 (2021).
352. Mounet, N. et al. Two-dimensional materials from high-throughput computational exfoliation of experimentally known compounds. *Nat. Nanotechnol.* **13**, 246–252 (2018).
353. Olsen, T. et al. Discovering two-dimensional topological insulators from high-throughput computations. *Phys. Rev. Mater.* **3**, 024005 (2019).
354. Marrazzo, A., Gibertini, M., Campi, D., Mounet, N. & Marzari, N. Relative abundance of Z_2 topological order in exfoliable two-dimensional insulators. *Nano Lett.* **19**, 8431–8440 (2019).
355. Wang, D. et al. Two-dimensional topological materials discovery by symmetry-indicator method. *Phys. Rev. B* **100**, 195108 (2019).
356. Sohncke, L. *Entwickelung einer Theorie der Krystallstruktur* (B. G. Teubner, 1879).
357. Fedorov, E. S. The symmetry of regular systems of figures. *Zap. Mineral. Obsc.* **28**, 28 (1891).
358. Shubnikov, A. et al. *Colored Symmetry* (Macmillan, 1964).
359. Gallego, S. V. et al. MAGNDATA: towards a database of magnetic structures. I. The commensurate case. *J. Appl. Crystallogr.* **49**, 1750–1776 (2016).
360. Gallego, S. V. et al. MAGNDATA: towards a database of magnetic structures. II. The incommensurate case. *J. Appl. Crystallogr.* **49**, 1941–1956 (2016).
361. Gallego, S. V., Tasci, E. S., de la Flor, G., Perez-Mato, J. M. & Aroyo, M. I. Magnetic symmetry in the Bilbao Crystallographic Server: a computer program to provide systematic absences of magnetic neutron diffraction. *J. Appl. Crystallogr.* **45**, 1236–1247 (2012).
362. Perez-Mato, J. et al. Symmetry-based computational tools for magnetic crystallography. *Annu. Rev. Mater. Res.* **45**, 217–248 (2015).
363. Cano, J., Bradlyn, B. & Vergniory, M. G. Multifold nodal points in magnetic materials. *Appl. Mater.* **7**, 101125 (2019).
364. Xu, S.-Y. et al. Hedgehog spin texture and Berry's phase tuning in a magnetic topological insulator. *Nat. Phys.* **8**, 616–622 (2012).
365. Belopolski, I. et al. Discovery of topological Weyl fermion lines and drumhead surface states in a room temperature magnet. *Science* **365**, 1278–1281 (2019).
366. Liu, D. F. et al. Magnetic Weyl semimetal phase in a Kagomé crystal. *Science* **365**, 1282–1285 (2019).
367. Morali, N. et al. Fermi-arc diversity on surface terminations of the magnetic Weyl semimetal $Co_3Sn_2S_2$. *Science* **365**, 1286–1291 (2019).
368. Xu, S.-Y. et al. Electrically switchable Berry curvature dipole in the monolayer topological insulator WTe_2. *Nat. Phys.* **14**, 900–906 (2018).
369. Cao, Y. et al. Unconventional superconductivity in magic-angle graphene superlattices. *Nature* **556**, 43–50 (2018).
370. Cao, Y. et al. Correlated insulator behaviour at half-filling in magic-angle graphene superlattices. *Nature* **556**, 80–84 (2018).
371. Lu, X. et al. Superconductors, orbital magnets and correlated states in magic-angle bilayer graphene. *Nature* **574**, 653–657 (2019).
372. Park, M. J., Kim, Y., Cho, G. Y. & Lee, S. Higher-order topological insulator in twisted bilayer graphene. *Phys. Rev. Lett.* **123**, 216803 (2019).
373. Xie, F., Song, Z., Lian, B. & Bernevig, B. A. Topology-bounded superfluid weight in twisted bilayer graphene. *Phys. Rev. Lett.* **124**, 167002 (2020).
374. Lian, B., Xie, F. & Bernevig, B. A. Landau level of fragile topology. *Phys. Rev. B* **102**, 041402 (2020).
375. Herzog-Arbeitman, J., Song, Z.-D., Regnault, N. & Bernevig, B. A. Hofstadter topology: noncrystalline topological materials at high flux. *Phys. Rev. Lett.* **125**, 236804 (2020).
376. Cao, Y. et al. Tunable correlated states and spin-polarized phases in twisted bilayer–bilayer graphene. *Nature* **583**, 215–220 (2020).
377. Jiang, Y. et al. Charge order and broken rotational symmetry in magic-angle twisted bilayer graphene. *Nature* **573**, 91–95 (2019).
378. Liu, X. et al. Tunable spin-polarized correlated states in twisted double bilayer graphene. *Nature* **583**, 221–225 (2020).
379. Xie, Y. et al. Spectroscopic signatures of many-body correlations in magic-angle twisted bilayer graphene. *Nature* **572**, 101–105 (2019).
380. Zondiner, U. et al. Cascade of phase transitions and Dirac revivals in magic-angle graphene. *Nature* **582**, 203–208 (2020).
381. Wong, D. et al. Cascade of electronic transitions in magic-angle twisted bilayer graphene. *Nature* **582**, 198–202 (2020).
382. Lu, X. et al. Multiple flat bands and topological Hofstadter butterfly in twisted bilayer graphene close to the second magic angle. *Proc. Natl Acad. Sci. USA* **118**, e2100006118 (2021).
383. Burg, G. W. et al. Evidence of emergent symmetry and valley Chern number in twisted double-bilayer graphene. Preprint at *arXiv* https://arxiv.org/2006.14000 (2020).
384. Anderson, P. W. Is there glue in cuprate superconductors? *Science* **316**, 1705–1707 (2007).
385. Shi, W. et al. A charge-density-wave topological semimetal. *Nat. Phys.* **17**, 381–387 (2021).
386. Wang, Z. & Zhang, S.-C. Chiral anomaly, charge density waves, and axion strings from Weyl semimetals. *Phys. Rev. B* **87**, 161107 (2013).
387. Laubach, M., Platt, C., Thomale, R., Neupert, T. & Rachel, S. Density wave instabilities and surface state evolution in interacting Weyl semimetals. *Phys. Rev. B* **94**, 241102 (2016).
388. You, Y., Cho, G. Y. & Hughes, T. L. Response properties of axion insulators and Weyl semimetals driven by screw dislocations and dynamical axion strings. *Phys. Rev. B* **94**, 085102 (2016).
389. Wieder, B. J., Lin, K.-S. & Bradlyn, B. Axionic band topology in inversion-symmetric Weyl-charge-density waves. *Phys. Rev. Res.* **2**, 042010 (2020).
390. Yu, J., Wieder, B. J. & Liu, C.-X. Dynamical piezomagnetic effect in time-reversal invariant Weyl semimetals with axionic charge-density waves. Preprint at *arXiv* https://arxiv.org/abs/2008.10620 (2020).

391. Lin, K.-S. & Bradlyn, B. Simulating higher-order topological insulators in density wave insulators. *Phys. Rev. B* **103**, 245107 (2021).
392. Li, X.-P. et al. Type-III Weyl semimetals: $(TaSe_4)_2I$. *Phys. Rev. B* **103**, L081402 (2021).
393. Gooth, J. et al. Axionic charge-density wave in the Weyl semimetal $(TaSe_4)_2I$. *Nature* **575**, 315–319 (2019).
394. Lee, J. M. et al. Stable flatbands, topology, and superconductivity of magic honeycomb networks. *Phys. Rev. Lett.* **124**, 137002 (2020).
395. Ritschel, T. et al. Orbital textures and charge density waves in transition metal dichalcogenides. *Nat. Phys.* **11**, 328–331 (2015).
396. Yu, R. et al. Quantized anomalous Hall effect in magnetic topological insulators. *Science* **329**, 61–64 (2010).
397. Chang, C.-Z. et al. Experimental observation of the quantum anomalous Hall effect in a magnetic topological insulator. *Science* **340**, 167–170 (2013).
398. Guin, S. N. et al. Anomalous Nernst effect beyond the magnetization scaling relation in the ferromagnetic Heusler compound Co_2MnGa. *NPG Asia Mater.* **11**, 16 (2019).
399. Ikhlas, M. et al. Large anomalous Nernst effect at room temperature in a chiral antiferromagnet. *Nat. Phys.* **13**, 1085–1090 (2017).
400. Sakai, A. et al. Giant anomalous Nernst effect and quantum-critical scaling in a ferromagnetic semimetal. *Nat. Phys.* **14**, 1119–1124 (2018).
401. Yang, H. et al. Giant anomalous Nernst effect in the magnetic Weyl semimetal $Co_3Sn_2S_2$. *Phys. Rev. Mater.* **4**, 024202 (2020).
402. Li, H. et al. Negative magnetoresistance in Dirac semimetal Cd_3As_2. *Nat. Commun.* **7**, 10301 (2016).
403. Ma, Q. et al. Direct optical detection of Weyl fermion chirality in a topological semimetal. *Nat. Phys.* **13**, 842–847 (2017).
404. Ji, Z. et al. Spatially dispersive circular photogalvanic effect in a Weyl semimetal. *Nat. Mater.* **18**, 955–962 (2019).
405. Nadj-Perge, S. et al. Observation of Majorana fermions in ferromagnetic atomic chains on a superconductor. *Science* **346**, 602–607 (2014).
406. Dalla Torre, E. G., He, Y. & Demler, E. Holographic maps of quasiparticle interference. *Nat. Phys.* **12**, 1052–1056 (2016).
407. Hsu, C.-H. et al. Topology on a new facet of bismuth. *Proc. Natl Acad. Sci. USA* **116**, 13255–13259 (2019).
408. Huang, S.-J., Song, H., Huang, Y.-P. & Hermele, M. Building crystalline topological phases from lower-dimensional states. *Phys. Rev. B* **96**, 205106 (2017).
409. Song, H., Huang, S.-J., Fu, L. & Hermele, M. Topological phases protected by point group symmetry. *Phys. Rev. X* **7**, 011020 (2017).
410. Lu, Y. F. et al. Zero-gap semiconductor to excitonic insulator transition in Ta_2NiSe_5. *Nat. Commun.* **8**, 14408 (2017).
411. Mazza, G. et al. Nature of symmetry breaking at the excitonic insulator transition: Ta_2NiSe_5. *Phys. Rev. Lett.* **124**, 197601 (2020).
412. Fleming, R. M., Sunshine, S. A., Chen, C. H., Schneemeyer, L. F. & Waszczak, J. V. Defect-inhibited incommensurate distortion in Ta_2NiSe_7. *Phys. Rev. B* **42**, 4954–4959 (1990).

Acknowledgements
This Review is dedicated to A. A. Soluyanov, who passed away during its preparation. B.J.W., N.R. and B.A.B. were supported by the Department of Energy (grant no. DE-SC0016239), the NSF EAGER (grant no. DMR 1643312), the NSF-MRSEC (grant no. DMR-142051), a Simons Investigator grant (grant no. 404513), the ONR (grant no. N00014-20-1-2303), the Packard Foundation, the Schmidt Fund for Innovative Research, the BSF Israel US Foundation (grant no. 2018226), the Gordon and Betty Moore Foundation (through grant no. GBMF8685 towards the Princeton theory programme), and a Guggenheim Fellowship from the John Simon Guggenheim Memorial Foundation. B.B. acknowledges the support of the Alfred P. Sloan Foundation and the National Science Foundation (grant no. DMR-1945058). J.C. acknowledges support from the National Science Foundation (grant no. DMR 1942447) and the Flatiron Institute, a division of the Simons Foundation. Z.W. was supported by the National Natural Science Foundation of China (grant no. 11974395), the Strategic Priority Research Program of the Chinese Academy of Sciences (CAS) (grant no. XDB33000000), and the Center for Materials Genome. M.G.V. acknowledges support from the DFG (grant no. INCIEN2019-000356), from Gipuzkoako Foru Aldundia and the Spanish Ministerio de Ciencia e Innovacion (grant no. PID2019-109905GB-C21). L.E. was supported by the Government of the Basque Country (project IT1301-19) and the Spanish Ministry of Science and Innovation (grant no. PID2019-106644GB-I00). C.F. was supported by the ERC (advanced grant nos. 291472 'Idea Heusler' and 742068 'TOPMAT'). T.N. acknowledges support from the European Union's Horizon 2020 Research and Innovation Program (grant no. ERC-StG-Neupert-757867-PARATOP). A.A.S. and T.N. additionally acknowledge support from the Swiss National Science Foundation (grant no. PP00P2_176877). L.E., N.R. and B.A.B. acknowledge additional support through the ERC Advanced Grant Superflat, and B.A.B. received additional support from the European Union's Horizon 2020 Research and Innovation Program (grant no. 101020833) and the Max Planck Society.

Author contributions
This Review was written and edited by B.J.W. All authors contributed to researching data for this article and to the preparation of the manuscript.

Competing interests
The authors declare no competing interests.

Publisher's note
Springer Nature remains neutral with regard to jurisdictional claims in published maps and institutional affiliations.

RELATED LINKS
BANDREP: https://www.cryst.ehu.es/cgi-bin/cryst/programs/bandrep.pl
Bilbao CrystallographicServer (BCS): https://www.cryst.ehu.es/
Catalogue of Topological Materials: http://materiae.iphy.ac.cn/
Check Topological Mat.: https://www.cryst.ehu.es/cryst/checktopologicalmat
ICSD 1559: https://www.topologicalquantumchemistry.com/#/detail/1559
ICSD 1560: https://www.topologicalquantumchemistry.com/#/detail/1560
ICSD 10017: https://www.topologicalquantumchemistry.com/#/detail/10017
ICSD 14348: https://www.topologicalquantumchemistry.com/#/detail/14348
ICSD 14349: https://www.topologicalquantumchemistry.com/#/detail/14349
ICSD 15569: https://www.topologicalquantumchemistry.com/#/detail/15569
ICSD 15571: https://www.topologicalquantumchemistry.com/#/detail/15571
ICSD 16585: https://www.topologicalquantumchemistry.com/#/detail/16585
ICSD 23062: https://www.topologicalquantumchemistry.com/#/detail/23062
ICSD 24145: https://www.topologicalquantumchemistry.com/#/detail/24145
ICSD 26881: https://www.topologicalquantumchemistry.com/#/detail/26881
ICSD 35190: https://www.topologicalquantumchemistry.com/#/detail/35190
ICSD 39597: https://www.topologicalquantumchemistry.com/#/detail/39597
ICSD 42545: https://www.topologicalquantumchemistry.com/#/detail/42545
ICSD 52115: https://www.topologicalquantumchemistry.com/#/detail/52115
ICSD 54609: https://www.topologicalquantumchemistry.com/#/detail/54609
ICSD 56201: https://www.topologicalquantumchemistry.com/#/detail/56201
ICSD 56390: https://www.topologicalquantumchemistry.com/#/detail/56390
ICSD 58396: https://www.topologicalquantumchemistry.com/#/detail/58396
ICSD 58786: https://www.topologicalquantumchemistry.com/#/detail/58786
ICSD 61352: https://www.topologicalquantumchemistry.com/#/detail/61352
ICSD 62305: https://www.topologicalquantumchemistry.com/#/detail/62305
ICSD 64703: https://www.topologicalquantumchemistry.com/#/detail/64703
ICSD 74704: https://www.topologicalquantumchemistry.com/#/detail/74704
ICSD 76455: https://www.topologicalquantumchemistry.com/#/detail/76455
ICSD 76139: https://www.topologicalquantumchemistry.com/#/detail/76139
ICSD 77109: https://www.topologicalquantumchemistry.com/#/detail/77109
ICSD 79233: https://www.topologicalquantumchemistry.com/#/detail/79233
ICSD 81218: https://www.topologicalquantumchemistry.com/#/detail/81218
ICSD 81493: https://www.topologicalquantumchemistry.com/#/detail/81493
ICSD 82092: https://www.topologicalquantumchemistry.com/#/detail/82092
ICSD 85507: https://www.topologicalquantumchemistry.com/#/detail/85507
ICSD 105699: https://www.topologicalquantumchemistry.com/#/detail/105699
ICSD 150530: https://www.topologicalquantumchemistry.com/#/detail/150530
ICSD 151748: https://www.topologicalquantumchemistry.com/#/detail/151748
ICSD 166865: https://www.topologicalquantumchemistry.com/#/detail/166865
ICSD 167811: https://www.topologicalquantumchemistry.com/#/detail/167811
ICSD 185808: https://www.topologicalquantumchemistry.com/#/detail/185808
ICSD 187534: https://www.topologicalquantumchemistry.com/#/detail/187534
ICSD 193346: https://www.topologicalquantumchemistry.com/#/detail/193346
ICSD 260148: https://www.topologicalquantumchemistry.com/#/detail/260148
ICSD 260982: https://www.topologicalquantumchemistry.com/#/detail/260982
ICSD 261111: https://www.topologicalquantumchemistry.com/#/detail/261111
ICSD 425966: https://www.topologicalquantumchemistry.com/#/detail/425966
ICSD 426972: https://www.topologicalquantumchemistry.com/#/detail/426972
ICSD 601065: https://www.topologicalquantumchemistry.com/#/detail/601065
ICSD 601659: https://www.topologicalquantumchemistry.com/#/detail/601659
ICSD 602710: https://www.topologicalquantumchemistry.com/#/detail/602710
ICSD 609930: https://www.topologicalquantumchemistry.com/#/detail/609930
ICSD 611451: https://www.topologicalquantumchemistry.com/#/detail/611451
ICSD 615755: https://www.topologicalquantumchemistry.com/#/detail/615755
ICSD 616956: https://www.topologicalquantumchemistry.com/#/detail/616956
ICSD 617192: https://www.topologicalquantumchemistry.com/#/detail/617192
ICSD 626175: https://www.topologicalquantumchemistry.com/#/detail/626175
ICSD 635132: https://www.topologicalquantumchemistry.com/#/detail/635132
ICSD 644091: https://www.topologicalquantumchemistry.com/#/detail/644091
ICSD 649753: https://www.topologicalquantumchemistry.com/#/detail/649753
ICSD 648185: https://www.topologicalquantumchemistry.com/#/detail/648185
ICSD 648570: https://www.topologicalquantumchemistry.com/#/detail/648570
ICSD 648585: https://www.topologicalquantumchemistry.com/#/detail/648585
ICSD 648588: https://www.topologicalquantumchemistry.com/#/detail/648588
ICSD 650381: https://www.topologicalquantumchemistry.com/#/detail/650381
ICSD 672362: https://www.topologicalquantumchemistry.com/#/detail/672362
ICSD 672345: https://www.topologicalquantumchemistry.com/#/detail/672345
ICSD 672522: https://www.topologicalquantumchemistry.com/#/detail/672522
Inorganic Crystal Structure Database (ICSD): https://icsd.products.fiz-karlsruhe.de/
Materials Project: https://materialsproject.org/
REPRESENTATIONS DSG: http://www.cryst.ehu.es/cgi-bin/cryst/programs/representations.pl?tipogrupo=dbg
Topological Materials Arsenal: https://ccmp.nju.edu.cn/
Topological Materials Database: https://www.topologicalquantumchemistry.com/
VASP2Trace: https://github.com/zjwang11/irvsp